Mathematisch-Naturwissenschaftliche Fakultät
der
Brandenburgisch Technischen Universität Cottbus

Diplomarbeit

Instabilities in ion thrusters by plasma-wall interactions

Julia Duras
Greifswald, den 22. August 2011

Gutachter:
Prof. Dr. Michael Bestehorn, Brandenburgisch Technische Universität Cottbus
Prof. Dr. Ralf Schneider, Ernst Moritz Arndt Universität Greifswald

Eidesstattliche Erklärung

Hiermit versichere ich, dass ich die vorliegende Arbeit selbständig verfasst und keine anderen Hilfsmittel als die angegebenen verwendet habe. Die Stellen, die anderen Werken dem Wortlaut oder dem Sinne nach entnommen sind, habe ich in jedem Falle durch Angaben der Quelle, auch der Sekundärliteratur, als Entlehnung kenntlich gemacht.

Greifswald, den 19.08.2010

Contents

1. Introduction

Plasma physics is covering a wide field of phenomena and technical applications, for example nebulae in the outer space, atomic fusion and medical applications. Non-linear physics is a basic characteristic of plasmas, leading to instabilities and turbulence. The transport related to this is a key question not only for ion thrusters, which will be addressed in this work, but also for fusion plasmas, determining the ultimate size of fusion reactors. Turbulence is a hot topic at the forefront of modern physics and far from being understood.

This thesis deals with is the ion thruster, a propulsion system for the outer space. Nowadays, the focus of ion thruster optimization lays on the investigation of plasma instabilities. They can lead to an anomalous diffusion to the thruster walls which means energy loss and reduced effectivity resulting in higher costs. The second challenge in plasma physics is the understanding of the interaction of plasmas with material boundaries, especially interactions between plasma and walls, like development of plasma sheath, sputtering or secondary electron emission. This topic will also be addressed in this thesis and one possible connection between turbulence and wall effects will be presented. To investigate plasma wall interactions computer simulations are useful, because they can easily analyze effects on small time and length scale and can switch physics on or off to investigate their effect. However, one should keep in mind that simulations are always just an approximation of the real physics and can be therefor just an addition to experiments.

In the first chapter a short introduction into the basic physics of propulsion systems and plasma physics will be given. Here the focus lies on the the plasma sheath in front of a plasma limiting wall and its behavior under secondary electron emission. Simulations of plasma sheath with and without secondary electron emission will be shown.

The second chapter deals with the operational principles of two kind of ion thrusters. Here different ion thruster concepts and their operational principles for the different regions, thruster channel and thruster plume, are discussed. The problem of plasma-wall interaction is a key issue for the operation and will be discussed in detail.

In the last chapter plasma instabilities will be discussed. The non linear dependencies of the plasma sheath and how it causes turbulences in the plasma bulk will be described. The production of plasma instabilities due to strong secondary electron emission will be analyzed for one thruster type to demonstrate how wall instabilities can affect the global plasma performance and the bulk turbulence. A self-consistent 3D simulation of a HEMP thruster model will show that electrostatic turbulences appears also for studies without SEE. For this simulation, an evaluation of a parallel matrix solver was done.

2. Basic physics

In this chapter the basic physics for this thesis are given. At first the physics of propulsion systems and a short introduction into plasma physics will be presented. Afterwards the physics of the plasma sheath in front of a plasma limiting wall and the mechanism of particle sputtering is shown.

2.1. Basic principles of propulsion systems for space missions

The velocity of a rocket with a constant exhaust depends on its mass. The change of velocity due to propulsion combustion is expressed in the rocket equation [1]. Consider a rocket, with a constant exhaust velocity v_e and a starting mass m_0. Let the initial mass m_0 be decreased by dm, due to propellant combustion. The ejection of the propellant mass $-dm$ with the velocity v_e produces an accelerating thrust $dp = -dm \cdot v_e$ on the rocket, which gains a velocity of $dv = -v_e \frac{\mathrm{d}m}{m}$. Integration brings $v = v_e \ln \frac{C}{m}$, with an integration constant C. For the initial condition $v(m = m_0) = 0$, one finds

$$v(m) = -v_e \; ln(\frac{m_0}{m}) \quad .$$

While in space missions a machine care is not economic, the lifetime of a thruster influences the maneuver distance. The distance is given as the produced thrust integrated over the lifetime. For ion thrusters the exhaust velocity v_e is nearly constant so that the thrust, given by Newton's third law, is mainly driven by the variation of the propellant mass in time

$$T = \dot{p} = \dot{m} v_e + m \dot{v}_e \approx \dot{m} v_e \quad .$$

For chemical thrusters the exhaust velocity is limited to approximately $3000 m/s$. To gain a higher thrust it is necessary to increase the maximum velocity. This can be done by electric propulsions, where charged particles get accelerated by electrical fields. The most simple concept of an electric propulsion system is the grid thruster. Here a radio frequency electric field ionizes a gas in a chamber and a charged grid at the thruster exit accelerates the produced ions. Since ionization and acceleration are independent of each other, it is possible to optimize these two quantities separately. This gives a high efficiency of grid thruster. But the impinging ions lead to a strong erosion of the grids. This limits the lifetime of the thruster, which makes it uneconomical for applications. To minimize the erosion, the next generations of ion thruster follow grid less concepts. While all ion thrusters accelerate charged particles, the performance of a thruster is determined by plasma physics.

2.2. Basic principles of plasma physics

In all ion thruster models, electric and magnetic fields guide, accelerate and trap plasma particles.
A plasma is an ionized gas, composed of electrons and ions of different charge. In this work, these particle species will be indicated with index s. In equilibrated plasmas, every specie has a Maxwell-Boltzmann distribution

$$f_s(\vec{v}) = \left(\frac{m_s}{2\pi k_B T_s}\right)^{3/2} exp\left\{\frac{-m_s v^2}{2k_B T_s}\right\} \tag{2.2.1}$$

with respect to the value of the velocity $v = |\vec{v}|$

$$f_s(v) = 4\pi v^2 \left(\frac{m_s}{2\pi k_B T_s}\right)^{3/2} exp\left\{\frac{-m_s v^2}{2k_B T_s}\right\} \quad , \tag{2.2.2}$$

the average velocity value

$$\langle v_s \rangle = \sqrt{\frac{8k_B T_s}{\pi m_s}} \tag{2.2.3}$$

and the root-mean-square velocity

$$\sqrt{\langle v_s^2 \rangle} = \sqrt{3\frac{k_B T_s}{\pi m_s}} \quad . \tag{2.2.4}$$

Here k_B is the Boltzmann constant. With the density n_s, the random flux density Γ and the current density j onto a plane are given as

$$\Gamma_s = \frac{1}{4} n_s \langle v_s \rangle \quad , \quad j_s = q_s \Gamma_s \quad . \tag{2.2.5}$$

Due to higher mass of the ions and mostly lower temperature, the average electron velocity in a plasma is much larger than the one for the ions.
The electric fields, induced by the plasma particles, are shielded due to different charges. Charge separation exists only on length scales smaller than the Debye length

$$\lambda_{D,s} \quad = \quad \sqrt{\frac{\epsilon_0 k_B T_s}{n_s q^2}} \quad , \tag{2.2.6}$$

where ϵ_0 is the permittivity of free space. The shielding potential of a plasma particle with a charge q is given by the Debye-Hückel-potential

$$\phi(r) = \frac{q}{4\pi\epsilon_0 r} e^{-r/\lambda_D} \quad .$$

Both electrons and ions are contributing to the shielding, so that the total Debye length $\lambda_D^{-2} = \lambda_{D,e}^{-2} + \lambda_{D,i}^{-2}$, consists of the electron and ion Debye length.
On length scales larger than λ_D, an equilibrated plasma can be considered as neutral, or so called "quasi neutral". Here the densities of electrons and ions are nearly equal

$$n_0 \quad = \quad n_e = Z_i \cdot n_i \quad , \tag{2.2.7}$$

with the ion charge number Z_i. The potential of a plasma ϕ_{Pl} is constant. That gets clear, if one considers a negative or positive perturbation of the potential. The fast electrons will follow the potential slope and eradicate immediately the perturbation.
In spite of quasi neutrality, the plasma particles are following electromagnetic forces. The interaction of charged particles with electromagnetic fields is governed by the Lorenz force. For a particle of species s, with charge q_s and mass m_s, moving with a non relativistic velocity $\vec{v}$ in the presence of electric ($\vec{E}$) and magnetic ($\vec{B}$) fields, the equation of motion is given by

$$\dot{\vec{p}_s} = q_s(\vec{E} + \vec{v} \times \vec{B}) \quad .$$

For a static electric field $\dot{\vec{E}} = 0$, $\vec{B} = 0$, charged particles are getting accelerated parallel to the field, with a speedup of

$$\vec{a}_s = \frac{q_s}{m_s}\vec{E} \quad .$$

In a plasma, this acceleration leads to a charge separation. For a static magnetic field ($\dot{\vec{B}} = 0$, $\vec{E} = 0$), a plasma particle, with an initial velocity $\vec{v} = \vec{v}_{\perp,s} + \vec{v}_{||,s}$ is oscillating in the plane perpendicular to the magnetic field $\vec{B}$ with a cyclotron frequency $\omega_{c,s}$ and the so called Larmor radius $r_{L,s}$,

$$\omega_{c,s} = \frac{q_s|\vec{B}|}{m_s} \quad , \quad r_{L,s} = \frac{v_{\perp,s}}{\omega_{c,s}} \quad ,$$

and moves with $v_{||,s}$ along the magnetic field lines. Here $v_{||,s}$ and $v_{\perp,s}$ are the contribution of the initial velocity parallel and perpendicular to the magnetic field $\vec{B}$.
In ion thrusters electric and magnetic fields are coexisting. Here the particles follow a cycloidal trajectory with a net drift perpendicular to both fields with a constant drift velocity [2]

$$\vec{v}_d = \frac{\vec{E} \times \vec{B}}{\vec{B}^2} \quad .$$

In contrast to the acceleration by only electric fields, this drift is not charge separating. This $\vec{E} \times \vec{B}$-drift is also known as the "Hall effect". For parallel magnetic and electric field, the plasma particles are gyrating around the magnetic field lines, with velocity and direction given by the electric field. The field lines can be seen as wires, along which the particles can move, while the electric field gives the kinetic energy to move. Due to the different charge and the larger mass of the ions, the electrons gyrate with higher frequency and smaller radius in the opposite direction to the ions.
Another oscillation in a plasma is caused by small electron density perturbations. If a displacement of electrons, with respect to the ions, exists, the Coulomb force pulls them back, acting as a restoring force. This rapid plasma oscillation has

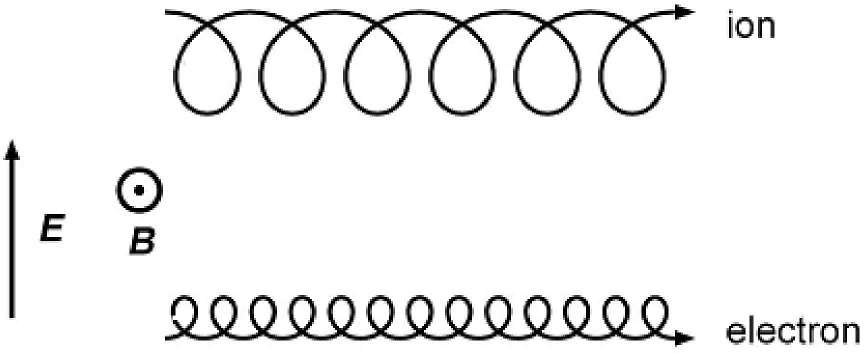

Figure 2.1.: Trajectories of ions and electrons in the presence of a magnetic field B and a perpendicular electric field E.

an angular frequency of

$$\omega_{p,e} = \sqrt{\frac{n_e e^2}{\epsilon_0 m_e}} \quad ,$$

also called plasma frequency.

2.3. Plasma wall contact

If an equilibrated plasma gets in contact with a grounded wall, in front of the wall a negative potential drop exists, which builds up a plasma sheath. In the bulk, the plasma can be seen as quasi-neutral. But next to a wall, charge separation, due to the much faster electrons appear and lead to a negative potential drop towards the wall. This potential drop influences the particle densities and velocities distributions. A plasma sheath is building up.

The main influence of the sheath characteristics is given by the physics property of the wall. Therefore the case of an ideal reflecting wall and the more realistic case of an electron emitting wall will be discussed.

In the simplest model of a plasma sheath only recombination at an ideal reflecting wall is assumed. Due to that, a sheath and a presheath is formed. In figure 2.2 a sketch of potential and density profile in the plasma sheath are shown. In the plasma bulk quasi-neutrality exists and the electron and ion densities are equal. While the velocity of the electrons is much higher than for the ions, more electrons than ions impinges on the wall. The electron density decreases near to the wall. This loss result in a negative potential near to the wall, which accelerates the ions. While the electron density is decreasing also the ion density decreases. For the steady-state, the result of the different velocities and densities are equal ion and electron flux at the wall.

$$\Gamma_e = \Gamma_i \quad .$$

The negative potential drop between plasma and wall, leads to accelerated ions in the sheath, while the electrons with an energy smaller than $e\Delta\phi$ are reflected. In the sheath the ions are still accelerated, while nearly all electrons are reflected. This leads to decreasing electron density at the wall, as shown in figure 2.2. The electron current density at the wall is then given by

$$j_e \quad = \quad -\frac{e}{4} n_e \left\langle v_e \right\rangle exp \left\{ \frac{-e\Delta\phi}{k_B T_e} \right\} \quad . \tag{2.3.1}$$

Also the ion density is decreasing within the sheath towards the wall, but not so strong, due to the negative wall potential. Close to the wall the impinging ions are neutralized by wall electrons. In this simple model, these neutrals are getting

reflected at the wall and getting ionized in the plasma, after an ionization length λ_{ion}, which is usually much longer than the sheath. Therefore, the sheath can be considered in many cases as collisionless.
A border of the sheath, the so called presheath is determined by the Bohm criterion. It says that the flow velocity of the instreaming ions at the sheath boundary is

$$v_{i,sh} \geq \sqrt{\frac{k_B T_e}{m_i}} = v_{Bohm} \quad ,$$

which is the ion sound speed. A derivation is given in appendix A.1. For zero net current at the wall ($j_e = j_i$) and quasi-neutrality ($Zn_i = n_e = n_0$), the drop

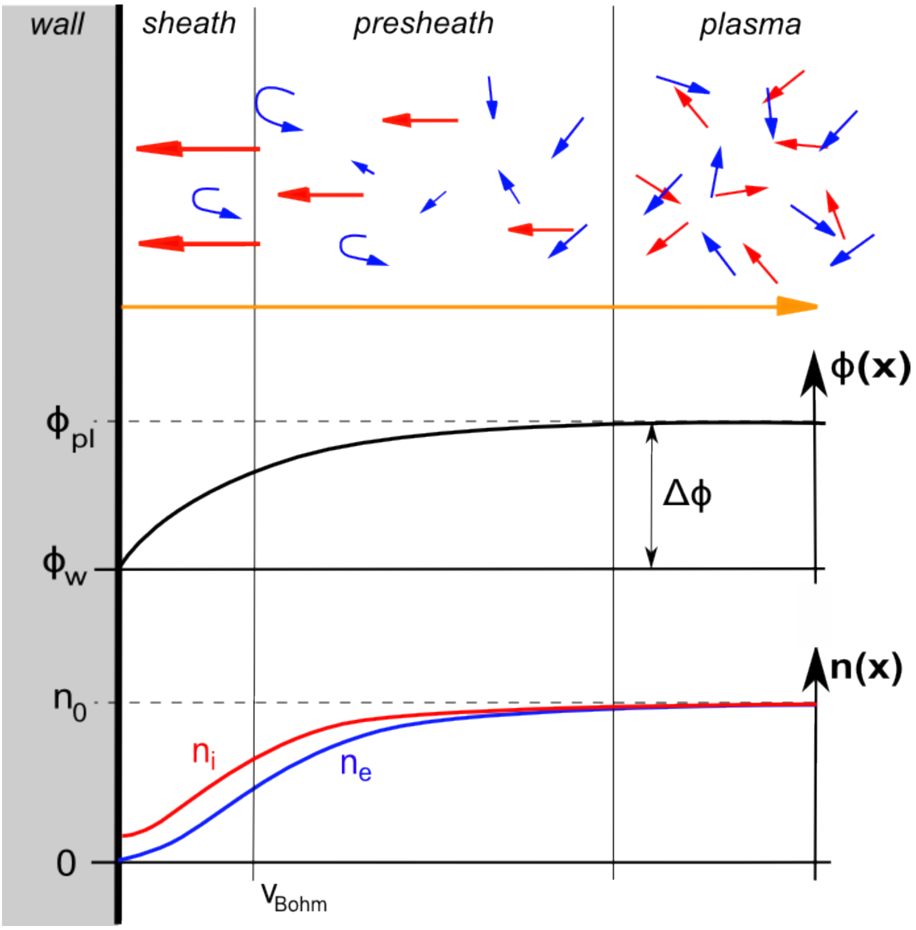

Figure 2.2.: Sketch of the important procedures in a plasma sheath. Red arrows represents electrons, blue ions and orange neutrals. At the bottom potential and particle densities are shown.

between plasma potential and wall potential can be estimated as [3]

$$e\Delta\phi \;\approx\; -k_B T_e \, ln\left(\sqrt{\frac{m_i}{2\pi m_e}}\right) \quad . \tag{2.3.2}$$

For an Argon plasma with single charged argon ions, this approximation gives a potential drop of about

$$e\Delta\phi \approx -4,68 \cdot k_B T_e$$

If we introduce secondary electron emission from the wall, the negative wall potential drop is reduced, because of the additional electrons coming from the wall reducing the electron flux density towards the wall. Therefore an effective potential drop [4]

$$e\Delta\phi^{eff} = -k_B T_e \ln\left[(1-\gamma)\sqrt{\frac{m_i}{2\pi m_e}}\right] \tag{2.3.3}$$

builds up, where the emission coefficient γ is defined as the ratio of the secondary electron emission flux to primary electron flux. The potential drop decreases with an increasing γ. In chapter 4 it will be shown, that an emission coefficient larger than a critical value γ_c will lead to an instable wall potential and hence induce anomalous diffusion.
Ions, depending on the material can also lead to the production of secondary electrons [5]. The produced electrons have low energy. This leads to a cooling of the plasma electrons, only energetic electrons get absorbed at the wall due to the negative wall potential. A steady plasma state with an electron density larger than zero builds up.
The velocity distribution function of electrons hitting the wall and emitted from the wall is not a Maxwellian distribution function [6].
To investigate a plasma sheath kinetic computer simulations are useful, like the Particle-in-Celle method, which was used here to simulate a plasma sheath next to an ion thruster channel wall.

2.4. Kinetic Simulation of a plasma (the Particle-in-Cell method)

"Particle-in-Cell" (PIC) is a simulation method, used for low temperature plasma studies. It gives a full self-consistent microscopic description of a plasma in position and velocity space and is able to involve complicated atomic and plasma-surface interactions. While it is impossible to calculate all particle-particle in-

teractions, the Poisson equation is solved on a grid, instead of calculating the Coulomb force between every particle. To calculate the potential from the Poisson equation, only the charge densities have to be known. Therefore the idea of PIC is to follow the motion of particles in a grid and calculate all macroscopic quantities at the grid points. For this reason, this simulation is called "Particle-in-Cell".
Since the number of charged particles in systems of interest is usually very large ($\geq 10^{12}$) it is impossible to perform particle simulations using the real particles even on the fastest computers. Instead of calculating the equation of motion

$$\dot{\vec{x}} = \vec{v} \tag{2.4.1}$$

$$\dot{\vec{v}} = \frac{q}{m}(\vec{E} + \vec{v} \times \vec{B}) \tag{2.4.2}$$

for each charged particle, PIC solves it for so called "super particles", representing thousands of real plasma particles. These super particles are following the same trajectories as the real plasma particles, due to the same ratio $\frac{q}{m}$. For a reliable plasma simulation, also effects on the smallest length scales $\lambda_{D,e}$ have to be resolved. Therefore the smallest lateral grid size is $\Delta x = 0.5\lambda_{D,e}$.

The smallest time steps of interests is the time is the electron plasma frequency. The time step between two PIC cycles is restricted to $\Delta t \leq \frac{2\pi}{\omega_{p,e}}$ and is taken as $\Delta t = 0.2\frac{2\pi}{\omega_{p,e}}$, which is the stability criterion of the numerical method, used to integrate the equation of motion in the particle mover.
A more detailed description of PIC can be found in [7].
The PIC simulation which is used in this thesis is an electrostatic simulation. That means only electric and static magnetic fields are calculated, while the effect of currents, leading to a magnetic field, are neglected. For a first investigation of plasma wall interactions a 1 dimensional simulation in space with a 3 dimensional resolution of the velocity were used. Here the lateral cut were made in the y-z-plane of a plasma vessel, so that the fluctuations in plasma parameters can be analyzed in the x-direction, perpendicular to the vessel walls. The simulated particle species in this simulation are electrons, single charged xenon ions and neutral xenon atoms. In the figure 2.3 the computational scheme is outlined. At first, the charge and current densities $\rho, \vec{j}$ are interpolated with a weighting function, from the particle positions x at the grid points X_j. With $j = 0, ..., N_g$, where N_g gives the number of grid cells for the 1 dimensional case. Then the Poisson equation

$$\nabla^2 \phi_j = -\frac{1}{\epsilon}\rho_j$$

is solved, on the grid to get the electric potential ϕ_j. Afterwards the electrical

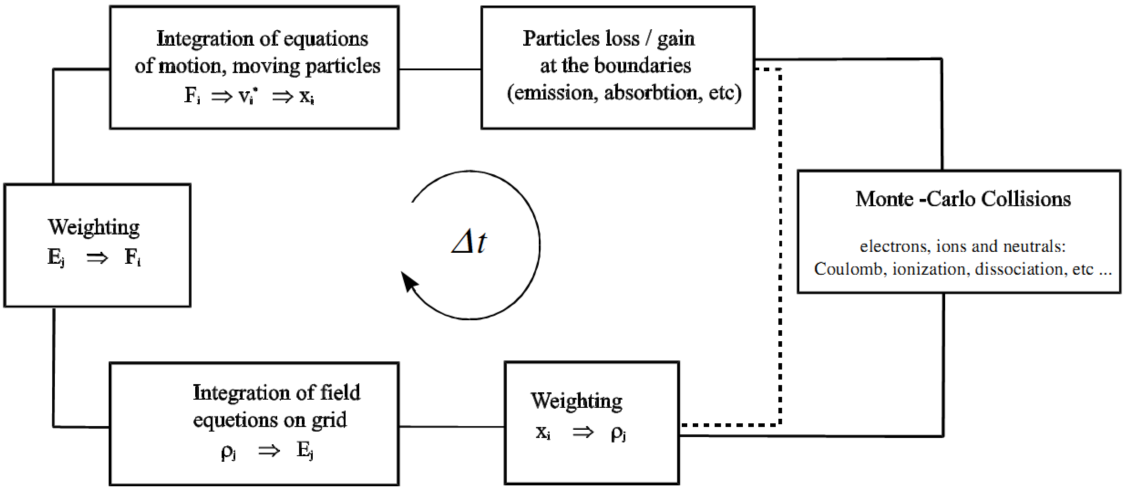

Figure 2.3.: PIC cycle

field values are interpolated from the grid points to particle positions. For the choice of the interpolation scheme, one has to take care that no self forces are generated. Now the equation of motion 2.4.1 for each super particle can be solved. In this numerical subunit, called "particle mover", boundary conditions have to be taken in account. After the movement of the particles, collisions are calculated. Now, for the next time step, the particle density can again be interpolated on the grid points and the PIC cycle is repeated. For an equilibrated plasma about 10^5 cycles has to be calculated. The PIC code gives the particle densities, potential, velocities and temperature in space, averaged over a given period.

2.4.1. The particle mover

Although the introduction of super particles reduces the number of simulated particles down to about 10^{10}, the solver of the equation of motion needs a high calculation speed. While the usual number of cycles is about $N_{PIC} \approx 10^4$, the solver needs also to ensure a high accuracy. In this thesis the Boris-Buneman integrator [8] is used. It is a method, optimized to solve the equation of motion of particles in electric and magnetic fields. It uses a leap frog scheme. That means, while the coordinates are calculated in the PIC time steps $n\Delta t, n \in [0, N_{PIC}+1]$

$$\vec{x}_{n+1} = \vec{x}_n + \Delta t \vec{v}_{n+1/2}$$

the velocities are calculated for times in between

$$\vec{v}_{n+1/2} = \vec{v}_{n-1/2} + \Delta t \frac{q}{m} (\vec{E}(\vec{x}_n) + \frac{\vec{v}_{n-1/2} + \vec{v}_{n+1/2}}{2} \times \vec{B}(\vec{x}_n)) \quad .$$

For a sufficient accuracy, the Boris-Buneman integrator requires $\omega_0 \Delta t \leq 0.2$ and a number of time steps $N_t \leq 10^7$ [6].
For a faster calculation, the particle mover can be calculated in parallel on different cores. Therefore the domain is divided in subdomains, so that every processor deals only with particle in its own subdomain. To prevent artifacts, if a particle is crossing the border of a subdomain, additional bookkeeping grid cells are added at the borders of the subdomains. For the one dimensional PIC simulation in this thesis, only one core is used, due to the small system size.

2.4.2. The solver

In the electrostatic case, the electric potential is determined by the Poisson equation, which is given for the one dimensional case as

$$-\frac{\partial^2}{\partial x^2}\phi(X_j) = \frac{1}{\epsilon_0}\rho(X_j) \quad , \tag{2.4.3}$$

where X_j gives the coordinate of the super particle j. The second order derivative can be approximated by a three point finite difference formula

$$\frac{\partial^2}{\partial x^2}\phi_j \cong \frac{\phi_{j+1} - 2\phi_j + \phi_{j-1}}{\Delta x^2} \quad , \tag{2.4.4}$$

where the index j indicates the grid point and Δx is the spatial distance between these points. Here the boundary conditions for a grounded thruster walls can easily be implemented with

$$\phi(0) = \phi_0 = 0 \qquad \phi(L_x) = \phi_{N_g} = 0 \quad . \tag{2.4.5}$$

For a dielectric wall, which is not grounded, the wall developing potential can be realized by simulating a volume of the dielectric material, where the outer wall, which is not in contact with the plasma is set to a fixed potential and at the interface to the dielectrics only the normal component of the electric field has to be set equal.
The advantage of the finite difference formula is the transformation of an differential equation into a matrix equation, which can easily be solved by numerical libraries. The most common library for C and Fortran codes is SuperLU, which is also used here. It is a solver of large, sparse, nonsymmetric systems of linear

equations on high performance machines by a LU decomposition with partial pivoting and triangular system solve through forward and back substitution. It is offered as a sequential, a multithreaded and a parallel version [9].
In the electrostatic case the Poisson equation 2.4.3 with the boundary conditions 2.4.3 and the approximation 2.4.4 leads to the following matrix equation:

$$\begin{aligned} \hat{\mathrm{A}}\vec{\phi} &= \vec{\rho'} \\ \begin{pmatrix} 2 & -1 & & \\ -1 & 2 & -1 & \\ & \ddots & \ddots & \ddots \\ & & -1 & 2 \end{pmatrix} \cdot \begin{pmatrix} \phi_0 = 0 \\ \phi_1 \\ \vdots \\ \phi_{N_g} = 0 \end{pmatrix} &= \begin{pmatrix} \rho'_0 \\ \rho'_1 \\ \vdots \\ \rho'_{N_g} \end{pmatrix} \end{aligned} \tag{2.4.6}$$

with $\rho'_j = -\frac{\Delta x^2}{\epsilon_0}\rho_j$. Since the matrix is not changing during the whole simulation, it is decomposed in an upper and a lower triangular matrix $\hat{\mathrm{A}} = \hat{\mathrm{L}}\hat{\mathrm{U}}$, only once at the beginning while it is solved backwards for a given right hand sides $\vec{\rho'}$ in every PIC cycle. That saves computation time, which is crucial especially for two and three dimensional simulations.
While the size of the matrix is given by the number of grid points N_g, time consumption of the solver strongly depends on the grid size. Especially for an increase in dimension, time consumption rises with a power of 2 or 3. For three dimensional PIC simulations, this calculation time is the most limiting factor for the domain size and resolution.
The component of the electric field on the grid points are then calculated calculated with a central difference scheme

$$E_j = \frac{\phi_{j-1} - \phi_{j+1}}{\Delta x} \quad .$$

In this 1D thruster mode, electrons and ions are absorbed. For the absorption, the particle was removed from memory, when it crosses the wall. This simple method causes no numerical artifacts [7]. For the reflection of neutrals the new coordinates were set as $x^{ref} = -x$ and $v_x^{ref} = -v_x$. Since the particle charge is zero, no artifacts are produced.

2.4.3. Particle and field weighting

In PIC, particles are moving in space, but the field equation can not be solved numerically at each space point. So the space domain is discretized on a grid and the Poisson equation is calculated only at the grid points X_j. For this calculation the charge density had to be known at these points. Therefore the particles have to be mapped on the grid points with a function $S(x_i - X_j)$, where X_j implements the grid point and x_i the position of particle i, so that the density at the grid point can be given as the sum of particle densities over all particles weighted by the weighting function

$$\rho_j = \sum_{i=1}^{N} q_i \cdot S(x_i - X_j) \quad .$$

In order to avoid numerical artifacts, this function has to fulfill isotropy of space, charge conservation and one condition to avoid self forces [6]. The weighting scheme which is used in this thesis is called Cloud in Cell and fulfills all the three requirements. It assigns the density to the two nearest grid points

$$S(x - X) \begin{cases} 1 - \frac{|x-X|}{\Delta x}, & \text{when } |x - X| < \Delta x \\ 0, & \text{else} \end{cases} \quad .$$

According to this weighting approach the charged particles are treated as "clouds"

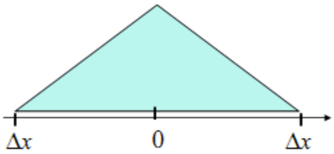

Figure 2.4.: Particle shape for the 1 dimensional Cloud in Celle weighting scheme.

with a dimension Δx and uniform charge density $\rho_i = \frac{q_i}{\Delta x}$, which can freely penetrate each other , therefore this scheme is called cloud-in-cell or CIC, and produces much less noise than a nearest-grid-point approximation [10].
After the Poisson equation has been solved at the grid points, the resulting electric fields E_j have to be mapped back on the particle coordinates. To conserve momentum, the same field weighting scheme has to be used like for the particle weighting.

2.4.4. Particle loading

Before the plasma simulation starts, the domain has to be filled with plasma particles. Also a continuous injection of particles has to be realized, to equalize the particle loss at the thruster walls.
To initialize the plasma, a 3-dimensional Gaussian velocity distribution $f(\vec{r})$ of electrons, single charged argon ions and neutral argon, randomly distributed

over the whole domain length L, were taken and sampled by an inverse Monte-Carlo sampling. A description of this method can be found in the appendix A.2. Neutrals are held at constant densities. For electrons and ions, a source of a flux of $\Gamma_h = 1.7 \cdot 10^{17} m^{-2} s^{-1}$ is added. Their velocity distribution is given by a 3-dimensional Gaussian weighted with its thermal velocity. While the background is reloaded with a random distribution over the whole domain, the heating source is placed at the middle of the domain.
Another loading of particles is the injection of secondary electrons at the thruster walls, which will be described in section 2.4.6.

2.4.5. Collisions

While in PIC the forces on particles is given only by macro-fields, it is necessary to implement extra collision routines. In the plasma of ion thrusters, inelastic Coulomb collisions between electrons and electrons, electrons and ions as well as elastic collisions between electrons and neutrals exist. While the exact interaction between particles scales with N^2, it is numerically too expensive to simulate all collisions. A choice of the colliding particles have to be taken, in order to minimize the number of collisions. One have to choose a method which resemble the overall effects of many small angle deflections. The weak Coulomb interaction for a particles distance larger than one Debye length is taken into account. Therefore particles are ordered according to their domain cells and then collided only with particles of the same cell [11].
For the frequent inelastic Coulomb collision, the scheme is simple: at first the particles of one cell are paired in a random way, than theses pairs (j, k) are statistically collided. Fortunately the Focker-Plank equation of a collision during a small time step can be a realized by a Gaussian distribution function of the scattering angle χ and a randomly distributed azimuthal angle ψ between $[0; 2\pi]$, so that χ and ψ can be sampled by an Monte-Carlo scheme. Then the corresponding rotational matrix $\hat{A}(\chi, \psi)$ gives the new direction of the collided particles. This is done for every grid cell during one PIC cycle.
For the less frequent elastic collisions between electrons and neutrals, a collision probability is given by

$$P(t) = 1 - exp\{-n \cdot E \cdot \sigma(v) \cdot t\} \quad .$$

Here the cross-section $\sigma(v)$, dependent on the incident velocity v, has to be calculated. The collision is taking place only if $P(t) \leq 1$. If that is the case, the incident velocity is reduced by the threshold energy E_{thr} and the rotational matrix and therefore the resulting velocities and directions after the collision, is calculated. For the ionization of the neutral by these electron-neutral collision, a new born ion-electron pair gets the position and velocity of the deleted neutral and the impinging electron collides again with the produced electron. These elastic collisions are also done only with particles in the same cell, and for every grid cell during one PIC cycle.

2.4.6. Injection of secondary electrons

In addition to the plasma source, an injection of electrons at the wall is introduced to simulate the secondary electron emission due to ion bombardment on the wall. When an ion impinges on the wall, the probability of the emission of a secondary electron is calculated. If the probability is smaller than 1, the number of ions are counted, until one secondary electron can be emitted. The emitted electron is placed at the wall with a constant velocity given by an energy of $2eV$, pointing into the plasma. This energy represents a typically value for low the low energy part of the distribution of secondary electrons [12].

2.5. Simulation of a plasma sheath

In this thesis a simulation of the plasma sheath next to a thruster wall was made to determine the influence of secondary electron emission (SEE) on the plasma sheath. To understand the general sheath behavior a one dimensional simulation without SEE was done first. Afterwards a weak SEE ($\gamma < \gamma_c$) was implemented, to study the static plasma sheath. In chapter 4, one, two and three dimensional PIC simulations of the plasma sheath next to a strong electron emitting wall ($\gamma > \gamma_c$) will be shown. For the one dimensional case, an argon plasma, as described above, was simulated. Here only electrons, single charged Argon ions and Argon atoms were considered.

In picture 2.5 the simulation results for the electric potential, density of electrons and argon ions and the electric current density in the plasma sheath in front of a grounded wall without SEE are shown. The grounded wall was implemented at $x = 0$ where the boundary condition were set as $\phi_w = 0$. The plasma source is set as $\Gamma = 1.7 \cdot 10^{17} m^{-2} s^{-1}$. The potential drop is here $\Delta\phi = 14V$. As predicted, the electron and ion densities are decreasing in the sheath due to the potential drop. The electron density at the wall is zero. While the positively charged ions, accelerated in the negative x-direction produce a positive current, the total current density $j_{tot,x} = j_{e,x} - j_{i,x}$ at the thruster wall ($x = 0$) is positive. The

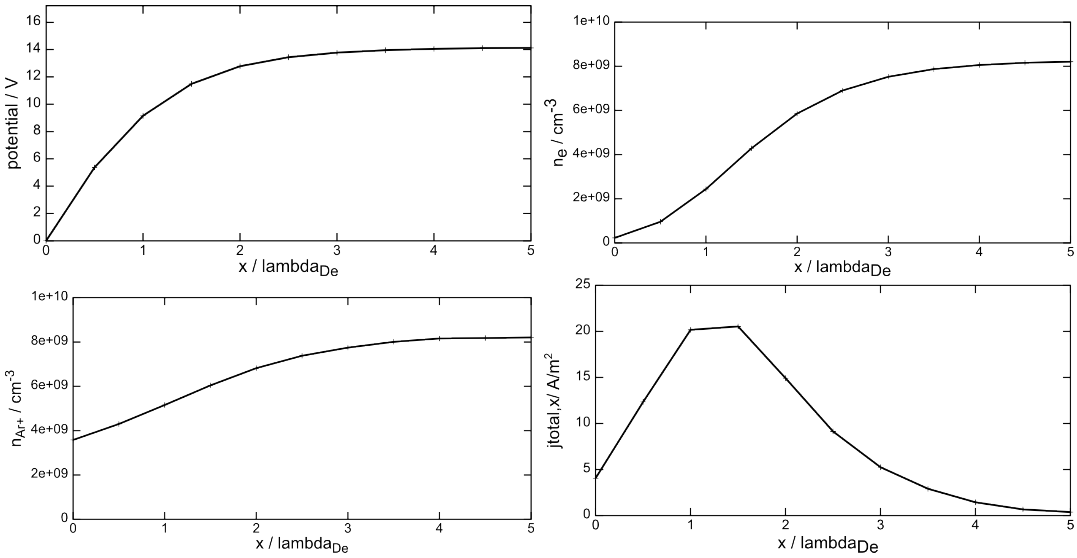

Figure 2.5.: PIC plot for plasma sheath in the stable regime with and without SEE.

electrons reflected from the wall are producing a positive current, therefore the current density is increasing at about one Debye length in front of the wall. After about $5\lambda_{D,e}$ the total flux is zero, due to quasi-neutrality.
In picture 2.6 a comparison of plasma sheath with SEE of $\gamma = 0.8$ (blue) and without SEE (black) is shown. One can see, that for the SEE case the electron

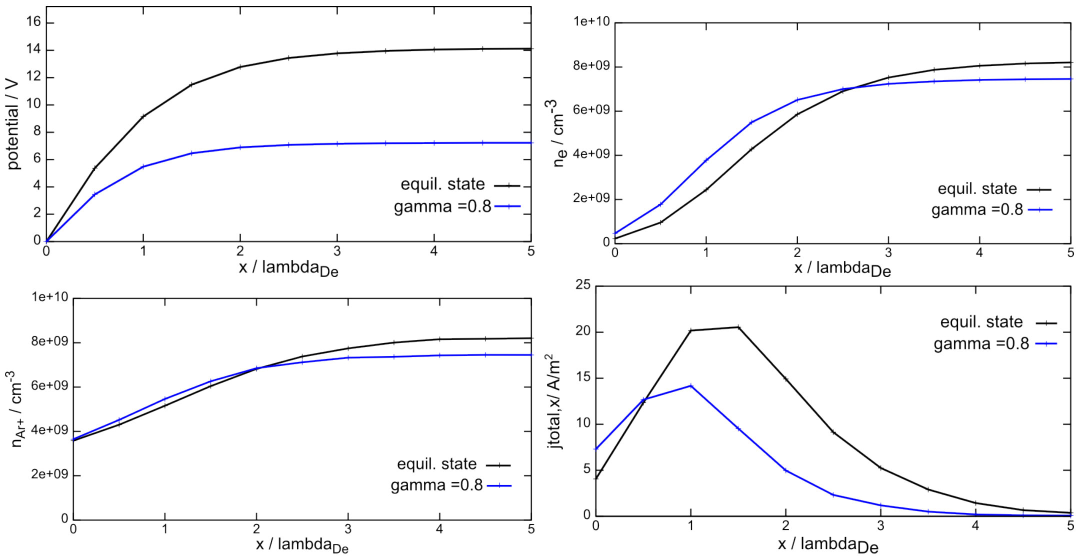

Figure 2.6.: PIC plot for plasma sheath in the stable regime with and without SEE.

density at the wall is larger. Therefore the total current density perpendicular to the wall is increasing at $x = 0$. The emitted secondary electrons producing a positive current, therefore the j_{total} in the whole sheath is decreasing until it also falls to zero at about $5\lambda_{D,e}$. Due to the SEE the potential drop is smaller than for the $\gamma = 0$ case. Due to different plasma sources, the plasma density of electrons and ions is smaller for the $\gamma = 0.8$ case.

2.6. Sputtering

Another plasma-wall interaction is sputtering, the knock out of particles from a solid target due to particle bombardment. The emitted particles can be target ions, atoms or target clusters. A good approximation of this process are binary collisions between the impinging ion, which gets neutralized next to the surface, and the target atoms, producing collisional cascades in the solid, as shown in picture 2.7. When a part of the collided particles get enough energy to leave the surface, the target emits them as sputtered particles. The sputter yield is given by the ratio between number of sputtered particles $N_{sp}(E)$, depending on the projectile energy E, and the number of projectiles N_p

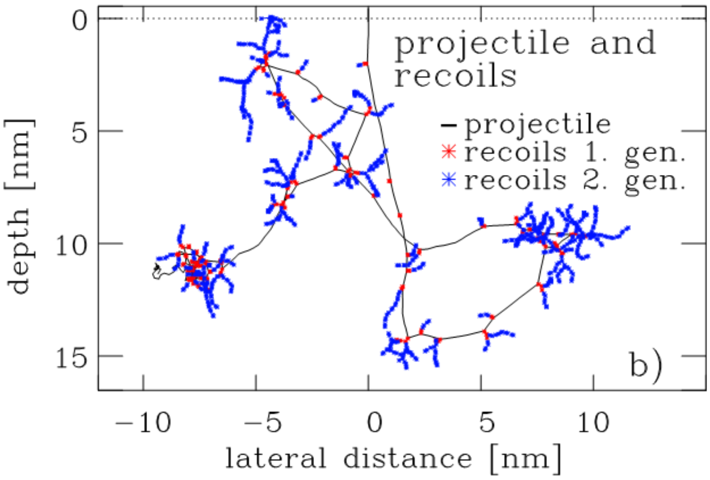

Figure 2.7.: Simulation of a trajectory (black) and generated recoils of first (red) and second generation (blue) of a $2keV$ He atom penetrating a Ni target at normal incidence [13].

$$Y(E) = \frac{N_{sp}(E)}{N_p} \quad , \tag{2.6.1}$$

and depends on the target and projectile species.
Sputtered particles are impurities in a plasma, values of sputter yields are important for plasma experiments and simulations. A tool for simulating binary collisions in matter is the SD.Trim.SP (Stationary/Dynamic Transport of Ions in Matter, with the calculation mode Serial or Parallel) code.

2.7. Simulation of Particles in Matter with the SD.Trim.SP code

The SD.Trim.SP computer program can be used to simulate sputtering, backscattering and transmission effects of ion bombarded material. It simulates collisional cascades in matter, with the so called Binary Collision Approximation (BCA).

2.7.1. Binary Collision Approximation

The Binary Collision Approximation (BCA) is the base of a range of computer simulation programs for interactions of ions or atoms with matter. A solid state is determined by its quantum mechanical solution of the many particle system, including temperature effects. Instead, the BCA treats the particle movement as a series of inelastic binary collisions between atoms.
The binary collisions between colliding atoms are calculated with the classical scattering integral for an incident energy of the projectile E_0 and an impact parameter p. The colliding partners are determined by the mean free path between two collisions and the impact parameter. The mean free path λ_{mfp} depends on the target density N with $\lambda_0 = N^{1/3}$. Therefore the distribution function is given as

$$f_1(\lambda)\mathrm{d}\lambda = \delta(\lambda - \lambda_0)\mathrm{d}\lambda \quad . \tag{2.7.1}$$

The impact parameter of a collision p, is determined by the scattering cross section σ. If one considers σ as a circle with the radius p_{max}, the maximum impact parameter, the distribution function for p is given by

$$f_2(p) = \frac{\mathrm{d}\sigma}{\sigma} = 2\frac{p}{p_{max}^2}\mathrm{d}p \quad , \tag{2.7.2}$$

with $\sigma = \pi p_{max}^2$ and $\mathrm{d}\sigma = 2\pi p\mathrm{d}p$. For the maximum impact parameter, the space between two collisions can be approximated as cylindrical volume, of hight

λ_{mfp}, radius p_{max} and density $N = (\pi p_{max}^2 \lambda_{mfp})^{-1}$, so that the maximum impact parameter results with $\lambda_{mfp} = N^{1/3}$,in

$$p_{max} = \pi^{-1/2} N^{-2/3} = 0.5642 \cdot N^{-2/3} \ .$$

Afterwards the scattering integral is solved and gives the scattering angle and the transfered energy from the projectile to the target atom. Also the time integral, which gives the duration of the collision, can be solved.

For projectile energies under $20eV$, the Binary Collision Approximation breaks down. Here chemical interactions of the incident atom with the matter is more important. This can be better simulated by Molecular Dynamic codes. A table of computer simulation programs which are using BCA, as well as references, can be found in [14].

2.7.2. The SD.Trim.SP code

For an amorphous structure of the target matter the SD.Trim.SP code was developed. It is based on the TRIM code and its dynamical version TRIDYN.

The SD.Trim.SP computer program simulates sputtering, backscattering and transmission effects of ion bombarded material and can additionally take the modification of the target into account, when it runs in the dynamic mode. It applies the Monte-Carlo BCA and assumes therefore an amorphous (randomized) material with a infinite lattice size and a temperature of $0K$. In SD.Trim.SP the particle movement in matter is approximated as a series of inelastic binary collisions between atoms, the BCA and a continuous friction, to simulate the interactions of moving atoms with electrons. For additional information about the use of SD.Trim.SP, see [13].

The domain of SD.Trim.SP, is a one dimensional simulation space, where the Cartesian x-component is perpendicular to the surface. Also two dimensional simulations are possible A negative x-component indicates the space above the surface, while a positive one shows the position in the matter. Also layers of different matter can be implemented.

SD.Trim.SP in static mode proceeds in the following way. At first a projectile is initialized with the kinetic energy E_0 and the direction $\vec{r_0}$. After a distance of λ, a collision partner is determined by the stochastic choice of an impact parameter p. While SD.Trim.SP assumes an amorphous structure of the material, no lattice structure has to be taken in account and therefore λ and p are determined by their distribution functions given by equation 2.7.1 and 2.7.2 of the BCA. Both are implemented with an inverse Monte-Carlo sampling. A description can be found in the appendix A.2. The azimuthal angles between two collisions are chosen randomly between $[0; 2\pi]$. The BCA gives the energies of the particles after the collision and the scattering angle ϑ_1 as well as the recoil angel ϑ_2, which are determining the new direction of the projectile and the target atom. The energy loss of atoms traveling through matter, due to interactions with electrons, is simulated as a continuous friction in between two collisions. The friction depends on the velocity of the projectile and is determined by a chosen interaction potential. Three scenarios are possible for each particle. If the energy is smaller than the binding energy of the matter $E < E_b$ the particle sticks and is not followed any more. If $E > E_b$ and the particle is close enough to the surface, it gets emitted as a sputtered atom and is also not followed any more. In the third case the particle moves through the matter and produces a collision cascade through several collisions, proceeded as described above. Reflection at the surface is realized with different binding energies for particles coming from inside or outside the target.

To determine the dynamics of the target thickness, SD.Trim.SP has a dynamic mode. Here the material is resolved one dimensional and the target is segmented into slabs. These slabs have an initial thickness, which is changing during the calculation, due to collisional transport.

For many particles, the calculation as well as the memory occupation of every collisional cascade becomes very costly. Therefore for large fluence, pseudo particles which are representing a number of real particles are introduced, to minimize the numerical costs. For an entire dose of Φ_0, the material should be exposed with, pseudo particle represents with a differential fluence of $\Delta\Phi = \Phi_0/N_d$ are calculated in N_d simulation steps.

An example of simulated sputter yield Y dependent on the incident energy E_0 for H bombardment on a Ni target, at normal incidence, can be seen in picture 2.8. One can see, that the sputter yield has a threshold energy E_{thr}. After wards Y is rapidly decreasing. For the shown case of hydrogen on nitrogen, for higher energies the yield is increasing. The light hydrogen is penetrating the target deeper with a higher energy. For more heavy projectiles the penetration depth would be smaller, which leads to a more flat dependence of the sputter yield on higher incident energy.

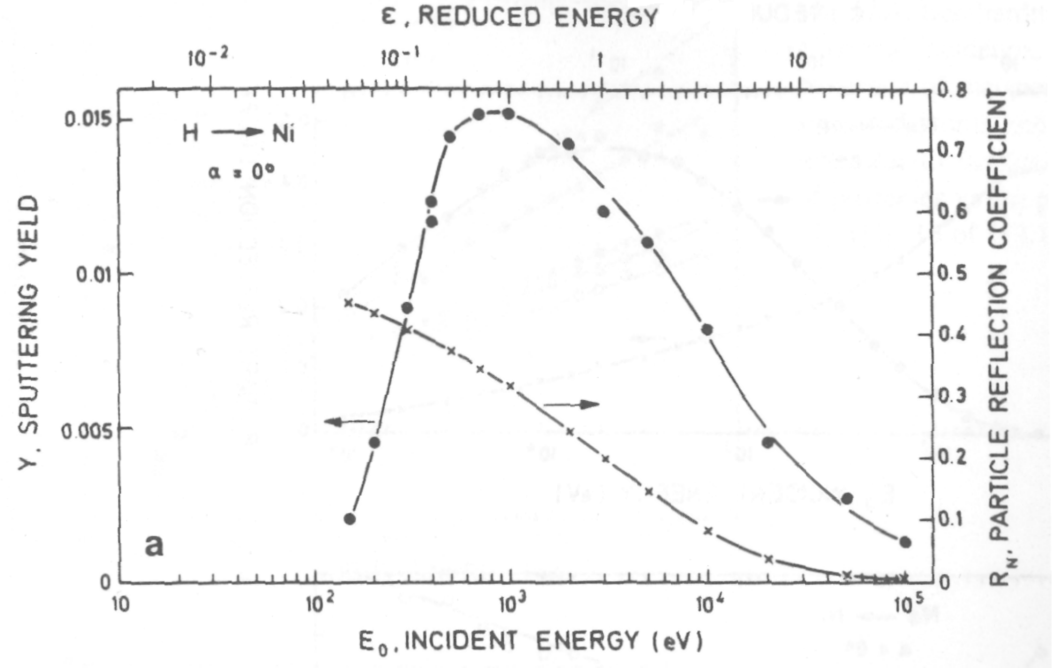

Figure 2.8.: Bombardment of Ni by H at normal incidence $\alpha = 0$. Calculated sputter yield Y and particle reflection coefficient R_N vs the projectile energy E_0. [14]

3. Operational principles of ion thruster

After the basic physics has been shown, different ion thruster concepts and their operational principles in the thruster channel region and the thruster plume region are discussed in this chapter. Plasma-wall interaction is a specifically criteria for the operation and will be discussed in detail.

3.1. Ion Thruster Concepts

In the field of electric propulsion systems, ion thrusters are getting more and more important for scientific and commercial space missions. Compared to the commonly used chemical thrusters they have a 5 to 10 times higher specific impulse [15]. Also their mass is much smaller, so that a significant reduction of spacecraft launch mass by some 100 to 1000 kg can be reached. As a consequence, commercial missions gain cost reductions and a larger flexibility in the choice of the launch rocket, whereas in case of scientific applications, missions deep into the solar system become possible.
In contrast to chemical thrusters, ion thrusters gain thrust by acceleration of heavy noble gas ions. The main types in applications or under development are radio frequency grid thrusters (RIT), Hall thrusters and High Efficiency Multistage Plasma Thrusters (HEMP-T). These three ion thruster concepts will be shortly explained in this chapter.

3.1.1. The grid thruster

The grid thruster type is one of the first build ion thrusters and was developed in the the early 1960's at the National Aeronautics and Space Administration, NASA. One thruster of this type is the Radio Frequency sustained Ion Thruster (RIT), as shown in figure 3.1. As it can be seen in the sketch, the grid thruster

consists of an ionization chamber terminated by two grids, surrounded by magnetic coils. The inner (screen) grid, is positively charged to confine the plasma, while the outer one (acceleration grid) is negatively charged to accelerate and extract the produced ions.
The magnetic coils are producing an alternating magnetic field, which induces

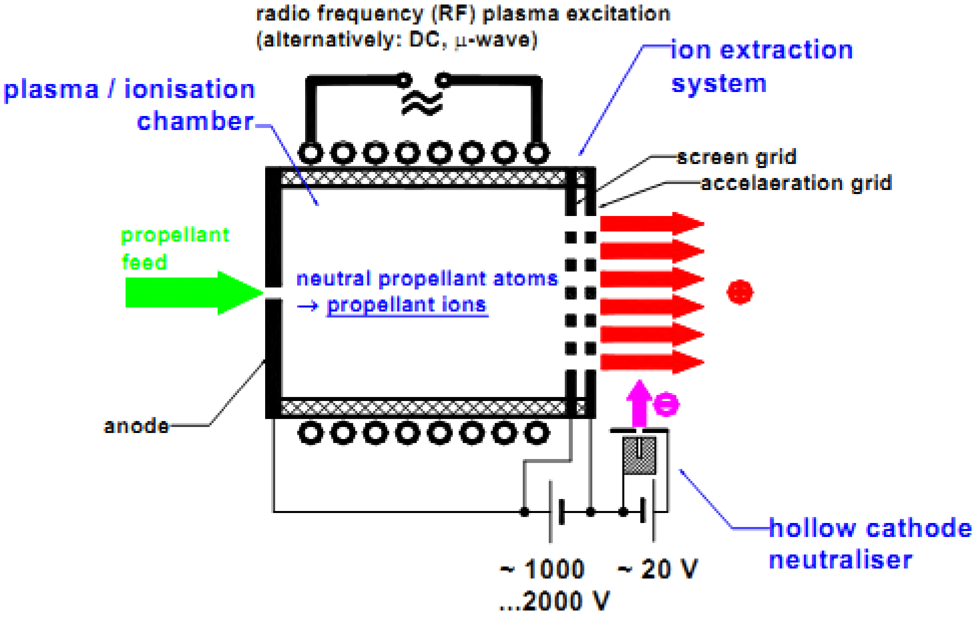

Figure 3.1.: Schematic view of Radio Frequency sustained Ion Thruster (RIT).

a radio frequency electric field. This field accelerates electrons in the chamber, so that they are colliding with the neutral gas atoms and ionize them. The positively charged ions move towards the grid system of the chamber. If ions enter the plasma sheath at a grid hole, they are getting accelerated by the potential difference between the first and the second grid and producing the thrust. Because the ionization is not taking place in that acceleration region, the acceleration potential drop can be optimized and is as steep as possible, to produce a high thrust.
Due to the grid erosion by ions, the lifetime of a grid thruster is quite low. For a longer lifetime, the next generation of ion thrusters, like the Hall thruster SPT, are grid-free concepts.

3.1.2. The Stationary Plasma Thruster (SPT)

One grid free concept is the Hall effect thruster, like the Stationary Plasma Thruster (SPT). It is currently the most used ion thruster and has performed

well on Astrium's geo-stationary Eurostar 3000 telecommunication satellite platform as well as on ESA's Smart-1 mission [15]. It also has been proposed for future satellite missions.
The operation principle of a Hall effect thruster is the Hall effect which traps electrons. The trapped electrons ionize the propellant gas and the produced ions get accelerated by a magnetic field. In picture 3.2 a schematic view of the SPT is shown. It consists of a ring shaped plasma channel, with an inner radius $R_{in} = 30mm$ and an outer radius $R_{out} = 50mm$ and a channel depth of $L = 25mm$. Permanent magnets (P) produce a radial magnetic field towards the inner walls while a static electric field (E), perpendicular to the magnetic field (B), is produced by an anode (A) and points outwards the thruster channel. Since the electrons are magnetic, the Hall effect traps them in a circular movement in the plasma channel. The neutral xenon gas Xe^0, exhausted at the channel bottom, gets ionized by collisions with these circulating electrons. The produced electrons are trapped in the plasma channel, due to the Hall effect. The generated positive ions are accelerated in the electric field, since they are only slightly affected by the magnetic field. They produce the thrust of the satellite. At the thruster exit an electron gun is placed. It neutralizes the xenon ions to avoid damage of the satellite. While the thruster is emitting positive

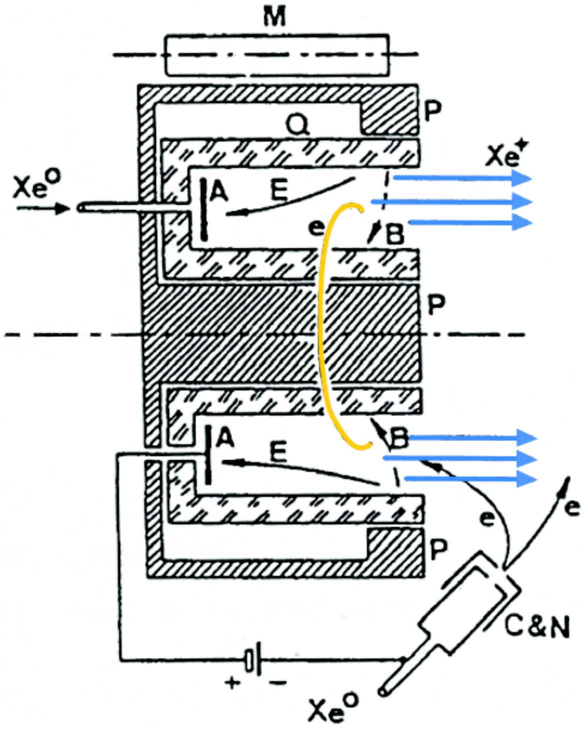

Figure 3.2.: Schematic view of the Stationary Plasma Thruster (SPT)

charged ions, the whole satellite gets negatively charged, which accelerates the ions toward the satellite. Especially the sensitive solar panels can be affected by that. Therefore, a neutralizer, acting also as primary source for electrons, is installed outside the thruster channel. The electron gun acts also as the primary electron source. Electrons emitted by that gun are attracted by the anode potential and fly towards the thruster channel, there they are trapped by the Hall effect. Additional radial transport processes lead to a transport perpendicular to the magnetic field, so that electrons are distributed over the whole channel. A discussion of the this will be given later in chapter 4.

The production of ions depends on the electron energy and should be in the range of $15 - 20eV$ for single charged xenon ions. To avoid higher charged ions, in order to reduce the damage of the satellite, highly energetic electrons have to be removed. In the SPT, this is done with SEE at the thruster walls. The negative potential drop of the plasma sheath next to the wall allows positive charged ions and highly energetic electrons impinge the wall, while the low energetic electrons are reflected. The impinging highly energetic electrons are absorbed, while the ions are producing lowly energetic secondary electrons. That lead to cutting-off of the highly energetic part of the distribution function, the average electron temperature decreases.

A better ionization rate in the thruster channel can be achieved with a larger amount of electrons. Therefore dielectric ceramic materials like BN, Al_2O_3 or SiO_2, with a larger yield of secondary electrons, are used for the SPT thruster walls.

Compared to the grid thruster, the lifetime is longer, about $1.000 - 2.000h$ in total. It is limited by the erosion of the truster inner walls. But due to a continuously potential drop in the channel, as will be discussed in section 3.2, the thrust of $\approx 2mN/cm^2$ is lower, than for a grid thruster.

3.1.3. The High Efficient Multistage Plasma Thruster (HEMP)

An ion thruster design which has the advantage of a strong potential drop, like the grid thruster model and an even longer lifetime than the SPT is the High Efficient Multistage Plasma Thruster (HEMP), patented by the THALES group in 1998 [16]. The sketch in picture 3.3 shows the cylindrical plasma thruster channel of HEMP. The anode at the bottom produces an axial electric field. At the thruster exit, a neutralizing electron gun is placed. The thruster channel has a radius of $9mm$ and a length of $43mm$. Instead of a radial magnetic field, an axial field is produced by a number of permanent magnets, facing each other in a repulsive way. Only at the regions between magnets, the so called cusps,

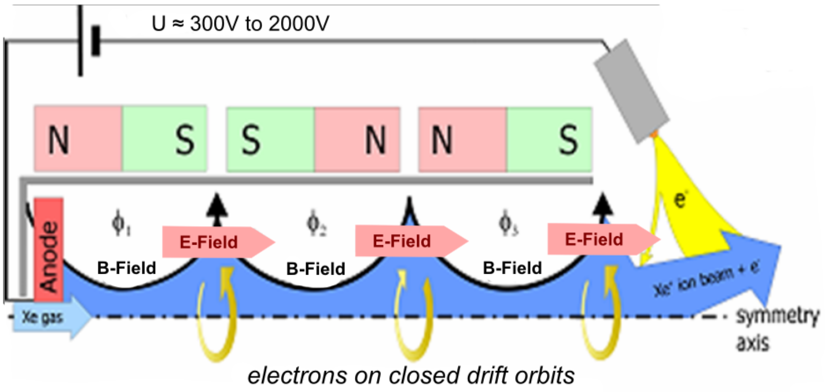

Figure 3.3.: Schematic view of the High Efficient Multistage Plasma Thruster (HEMP).

magnetic field lines are perpendicular to the walls and the electric field. Two cusp regions are existing, the anode cusp and the exit cusp. Because of the small operating distance of the cusps compared to the thruster diameter, an overall magnetic field pointing towards the thruster exit is building up. While in the SPT the whole channel is used to ionize the xenon gas, in the HEMP thruster the ionization takes place only at the cusps regions. Here the Hall effect traps the electrons and forces them to a radial motion. HEMP is characterized by a longer lifetime of about $5.000 - 10.000h$, which will be explained later. An other effect of the dense magnetic field lines at the cusps is the mirroring of the electrons. Here, the velocity of the electrons decreases with the density of the field lines so that they even can get reflected [2]. Thus the density of the electrons in the cusp regions is high and the ionization can take place efficiently. For the HEMP thruster the electron gun is the primary electron source. The transport of electrons perpendicular to the magnetic field lines, towards the exit cusp is caused by anomalous diffusion, as will be explained in section 4.

3.2. Operational characteristics of ion thrusters in the channel

The main difference between SPT and HEMP is the quantity of the electron wall contact induced by the different arrangement of the magnetic fields. How does that affect the plasma physics at the thruster walls?
In [17], potential, densities and temperature of the SPT and the HEMP were calculated with a 2d3v PIC simulation. Both simulations are handling electrons, single charged Xenon ions and Xenon atoms, covering the thruster channel and

the plume region. The inner surface of the channel walls are made of Boron Nitride and an initial electron temperature was set to $T_e = 2eV$.
In picture 3.4 and 3.5 the potential is shown. One can see that for the SPT, the potential profile is rather smooth and the major drop of about $270V$ is inside the channel. This is caused by the radial electric field. For the HEMP thruster the potential in the plasma bulk is nearly constant, which results in a steep drop at the thruster exit, producing a higher thrust than the SPT does. Here the mainly axial magnetic field allows the electrons to flow in parallel to the electric field. A small perturbation of the electric potential is therefore quickly compensated by fast electrons.

Near thruster walls, the potential of both thrusters is decreasing due to the zero net current at the wall. While for the SPT the radial magnetic field in the whole channel leads to a smooth potential drop towards the walls, the potential drop in the HEMP thruster has mostly a sharper decline. Here the electrons are following the axial magnetic field, so that the potential drop of the sheath

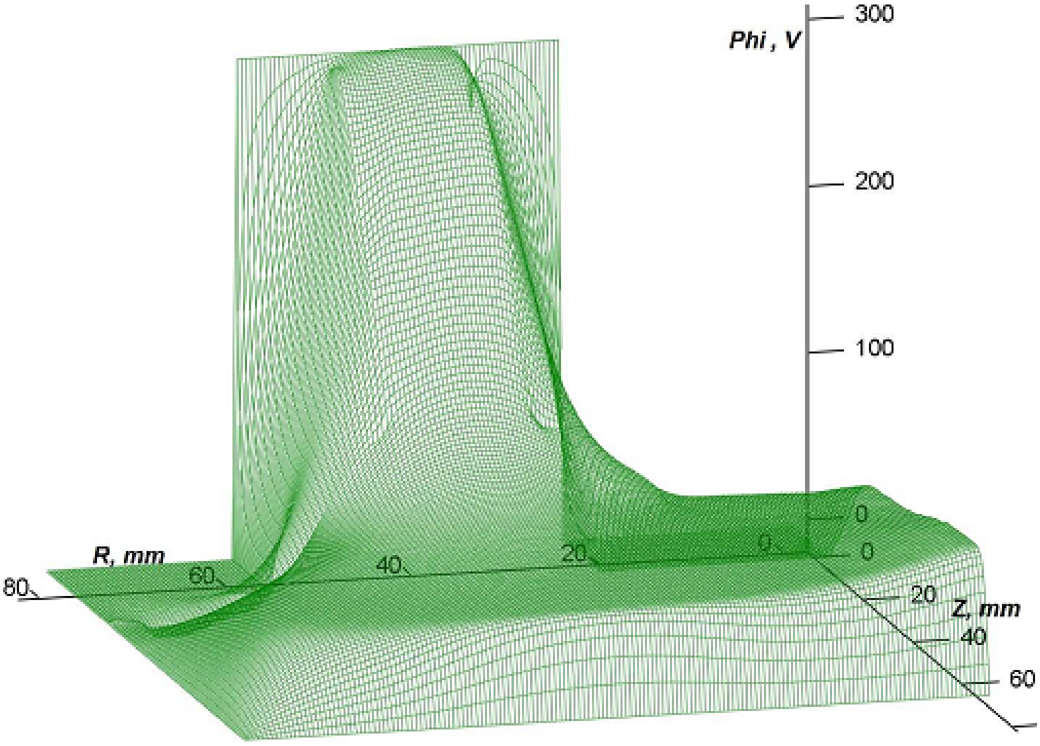

Figure 3.4.: Potential profile of the SPT100 ML thruster, calculated by [17]. The thruster channel has the inner and outer radii $R_{in} = 34.5mm$ and $R_{out} = 50.0mm$. The channel depth is $25mm$. The metal anode has a potential of $300V$.

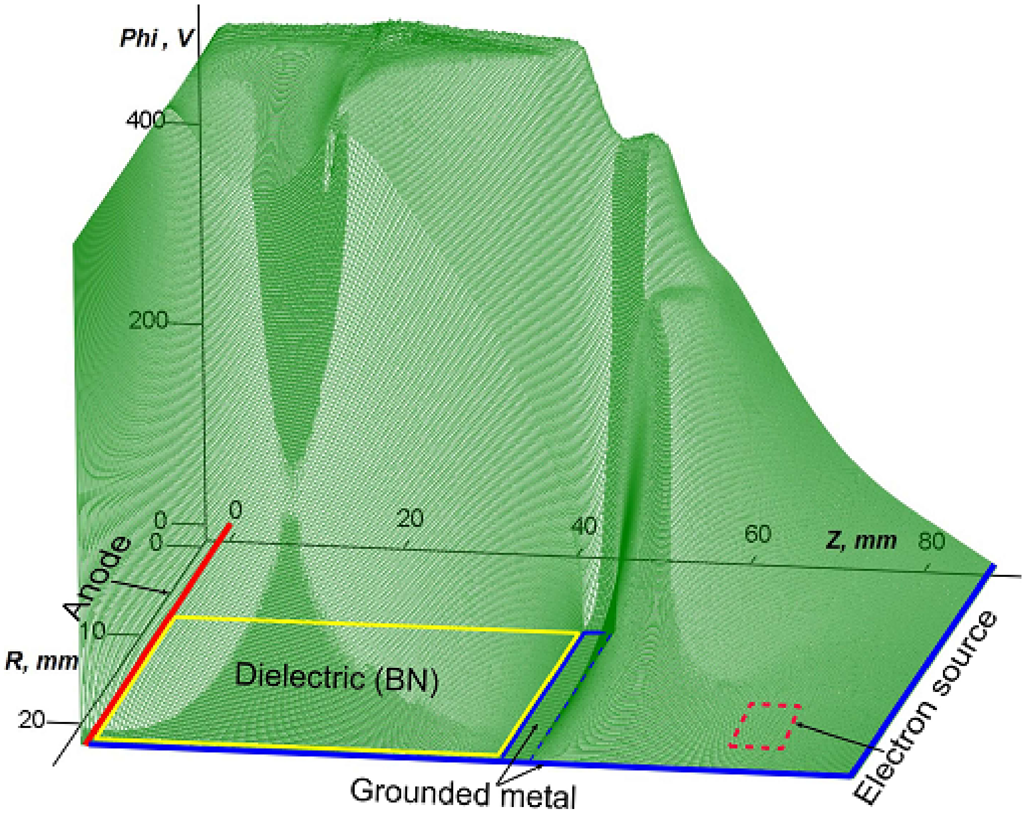

Figure 3.5.: Potential profile of the HEMP DM3a thruster, calculated by [17]. The computational domain for the simulation is shown in the plane. Thruster channel with radius $R = 9mm$ and length $L = 51$. The anode is set with $500V$.

is affecting them closer to the wall, as for a radial magnetic field. In the cusp region at about $z = 19mm$, the potential is dropping smoothly due to the radial $\vec{B}$ field.

The influence of the plasma sheath can also be seen in the electron density ins figure 3.6 and 3.7. For the SPT the electron density is uniformly decreasing towards the channel walls. For the HEMP thruster this is also the case. In addition the cusp region can be verified. Here the stronger plasma wall contact takes place so that the electron density reaches the channel wall early.

The higher electron density in this region due to magnetic mirroring at the dense magnetic field lines is visible. In picture 3.5 the potential drop due to the plasma-wall interaction can be seen.

Also sputtering of the wall material by the impinging ions takes place in the

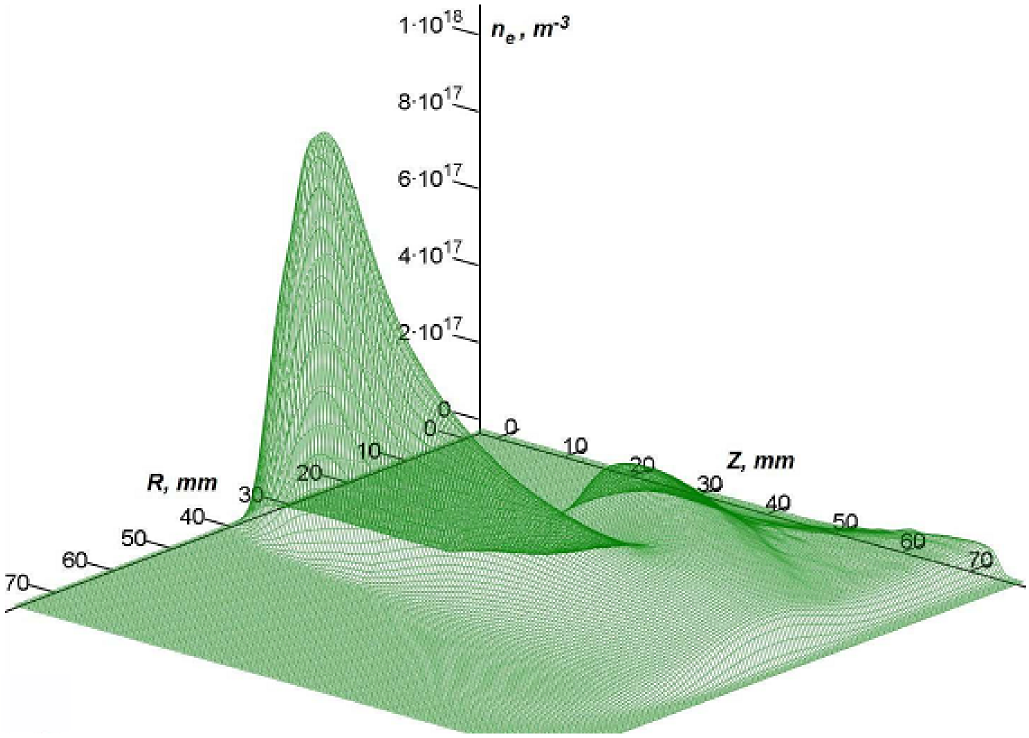

Figure 3.6.: Electron density profile of the SPT100 ML thruster, calculated by [17]. The thruster channel has the inner and outer radii $R_{in} = 34.5mm$ and $R_{out} = 50.0mm$ and a channel depth of $25mm$. The metal anode has a potential of $300V$.

thruster channel. For ion thrusters sputtering over a long time can change the highly optimized geometry. That means changes of the potential appear, which lead to a different distributed exhaust and a different thrust. In [17] also the ion flux density to the wall dependent on the thruster channel depth z, as seen in figure 3.8 (left), was simulated. One can see, that for the SPT, the flux density to the walls is distributed over the whole thruster channel due to the radial magnetic field. For the HEMP thruster a four times higher peak appears, but only in the cusp region, where the strong plasma-wall interaction is taking place. But due to the low mean ion energy in this region, as shown on the right hand side, practically no erosion of the thruster takes place, as shown in figure 3.9. In contrast to that, the mean ion energy to the inner wall of the SPT is much higher than for the HEMP thruster, so that a strong erosion takes place. That explains the reduced life time of the SPT, compared with the HEMP thruster.

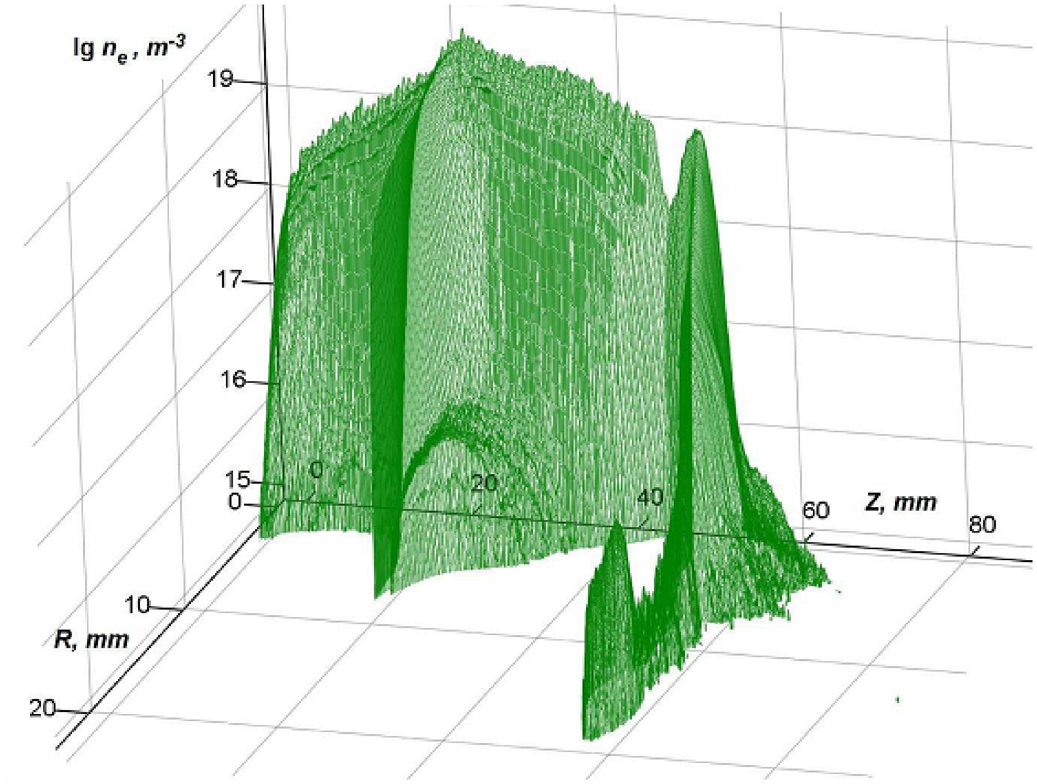

Figure 3.7.: Electron density profile of the HEMP DM3a thruster, calculated by [17]. The computational domain for the simulation is shown in the plane. Thruster channel with radius $R = 9mm$ and length $L = 51$. The anode is set with $500V$.

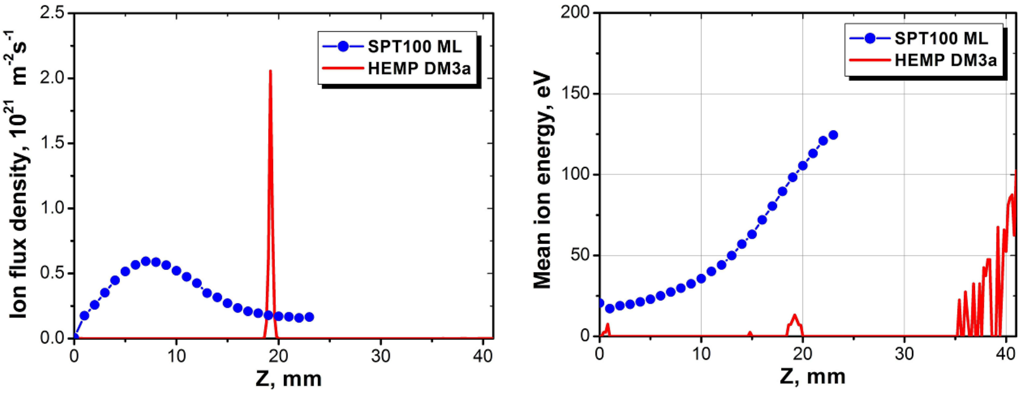

Figure 3.8.: The ion fluxes to the dielectric channel wall of the HEMP DM3a thruster and to the inner wall of the SPT100 ML (left); corresponding mean ion energy (right). [17]

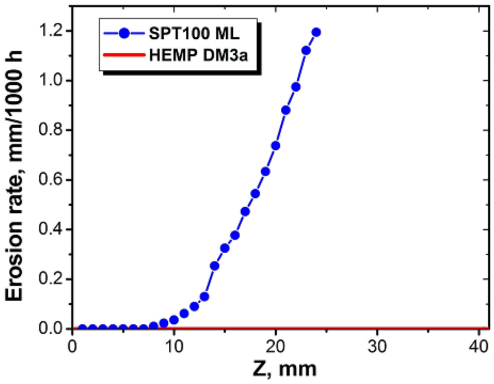

Figure 3.9.: The erosion rate for the dielectric channel wall of the HEMP DM3a thruster and for the inner wall of SPT100 ML as calculated with SDTrimSP. [17]

3.3. Operational characteristics of ion thrusters in the plume

The exhaust of the thruster is called plume. Here, the angular distribution of the exhausted ions and their speed determines the thrust of the satellite. The angular distribution can be influenced by the potential of the thruster exit plane, while the thrust is determined by the channel potential.

For the qualification of space missions, the thrusters have to be tested in large vacuum vessels for several 1000 hours. Although these vessels can be very large compared to the thrusters, the limited space of the vessel causes artifacts in the thrust measurement, which are not appearing in the outer space. During test runs , the accelerated thruster ions are eroding particles at the vessel walls by sputtering. This produces co-deposited layers every where in the test facility, also inside the thruster channel. Here these layers change the highly optimized geometry of the thruster and therefore the potential which accelerates the ions. For the qualification of HEMP, THALES was taking test runs at the Italian test facility Aerospazio Tecnologie. The utilized vacuum chamber is a cylinder of $8m$ length and has a radius of $2m$. The cylinder is closed by two spherical caps on its ends, as can be seen in the picture 3.10. The ion thruster was placed coaxial with the cylinder close to one of the ends. To investigate the artifacts during thruster measurements a qualitative analysis of the backscattered particles from the vessel walls to the thruster is needed. With this information the effect of the co-deposited layers inside the channel on the thrust and the angular distribution can been calculated.

Figure 3.10.: Photo of the vacuum chamber at Aerospazio Tecnologie.

The calculation of the back scattered particles were done with a direct Monte-Carlo simulation. For its validation, additional analytical calculations were done. In the following both models will be described. As a result, the angular distribution of the back scattered particles and the arrangements to provide such a back-flow will be shown.

3.3.1. Monte-Carlo simulation

In this simulation each exhausted ion of the thruster is followed, the sputter yield is calculated and each sputtered particle is followed as well. The resulting angular distribution of the back scattered particles is taken at the thruster exit. While all particles are generated with an inverse Monte-Carlo sampling of a given distribution (see appendix A.2), the simulation is called Monte-Carlo simulation. As sketched in figure 3.11, this procedure where done in three steps:

i) reproducing the angular distribution of the thruster particles

ii) calculating the number of eroded particles at the walls and their direction of flight

iii) collecting the back-flow to the thruster channel exit

In the first step an angular distribution of particles from a point source was realized by an inverse Monte-Carlo sampling. A typical current distribution for ion thrusters was chosen, as shown in 3.12(a). But also other distributions are possible. In the taken case, the plasma current density is defined on a distance

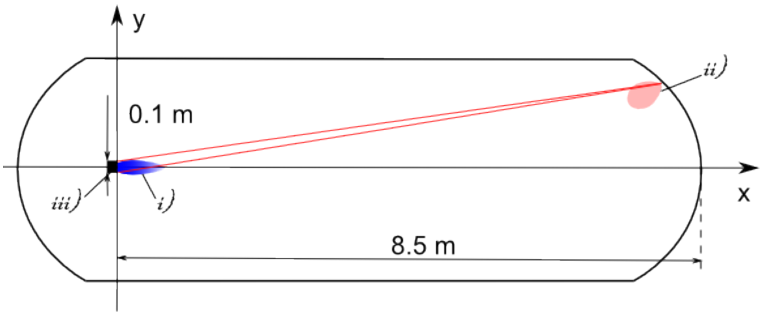

Figure 3.11.: Sketch of the Monte-Carlo simulation procedures (i-iii) and the dimensions of ion thruster and vacuum vessel.

of $1m$. The number of particles emitted in the solid angel $\mathrm{d}\Omega$ can be obtained as

$$\mathrm{d}N = \frac{I(\theta,\varphi)}{q}\mathrm{d}\Omega \quad , \tag{3.3.1}$$

where $I(\theta,\varphi)$ is the plasma current density in direction θ and φ and q the ion charge. While the thruster exhaust consists of single and double charged xenon ions, the fraction of Xe^{++} ions (α) have to be taken into account. Therefore a measured distribution of the Xe^{++} fraction, a shown in figure 3.12(b) was taken. For the number of Xe^{++} ions ($\mathrm{d}N^{++}$), the number of Xe^{+} ions ($\mathrm{d}N^{+}$) and the total number of ions ($\mathrm{d}N$) the current density will look like

$$I = \frac{e\cdot \mathrm{d}N^{+} + 2e\cdot N^{++}}{\mathrm{d}\Omega} \quad \Rightarrow \quad \mathrm{d}N = \frac{I}{e(1+\alpha}\mathrm{d}\Omega \quad ,$$

where e is the elementary charge. The energy of the sampled particles (E)can be given by a measured mean energy distribution $\tilde{E}$, shown in figure 3.12(c), as

$$E_{Xe^{+}} = \frac{\tilde{E}}{1+\alpha} \tag{3.3.2a}$$

$$E_{Xe^{++}} = \frac{2\tilde{E}}{1+\alpha} \quad . \tag{3.3.2b}$$

In the second step the intersection of the particle beam with the vessel was calculated. While no particle beam divergence within the volume were assumed, particle moving where calculated along rays. The amount of sputtered particles, dependent on the energy of the incident particle where calculated by a Monte-Carlo sampling. Therefore simulations of the sputter yields for different incident angles and energies were done with the SD.Trim.SP code. While only the value

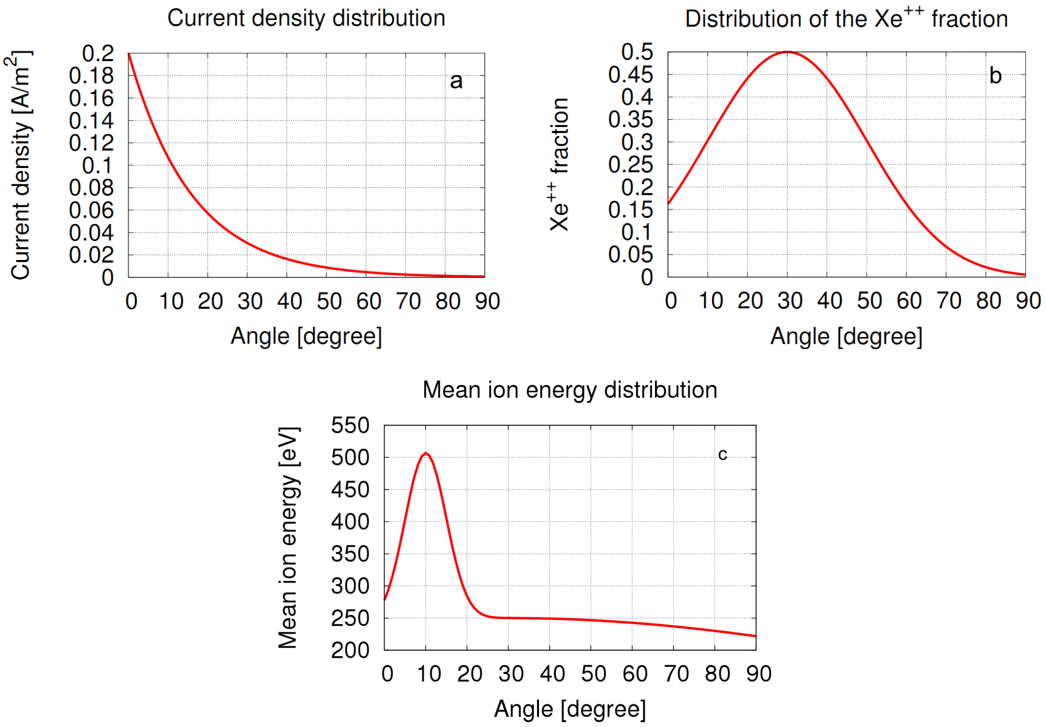

Figure 3.12.: Distribution of the total current density (a), the Xe^{++} fraction (b) and the mean energy (c) of exhausted ions of an arbitrary ion thruster, dependent on the angle of exhaust.

of $Y(E)$ is of interest, the simulation where run in the static mode. For the later investigation of the development of the co-deposited layers inside the thruster channel, the simulation is done with SD.Trim.SP in dynamic mode. For the angular distribution of the sputtered particles a cosine-distribution was used. In picture 3.13 one can see a simulated angular distribution of backscattered particles as a function of the cosine of the polar angle, calculated in [14]. For small angles of incidence α a cosine-distribution is sufficient where for larger ones it is not. But due to micro roughness of the wall surface large angles as well as very small ones are not appearing, because of shadowing.The cosine law is given as

$$dN_c = \frac{dN_i}{\pi} \cos \theta_{re} d\Omega \quad , \tag{3.3.3}$$

where dN_i is the flux of ions, dN_c is the sputtered flux, θ_{re} is the direction angle of the sputtered flux and $d\Omega$ is the solid angle in a direction of θ_{re}. For each impinging particle $10^2 \sim 10^3$ of the back scattered particles were simulated. The latter is done in order to speed up calculations, as only small portion of the back scattered particles come back to the collecting spot. For the same reason the sputtered particle weight is set equal to the sputtering yield. This allows to avoid sampling of the sputtering yield by the MC procedure.

In the last step the intersection of the eroded particles with the truster exit where calculated along rays and collected in a histogram.

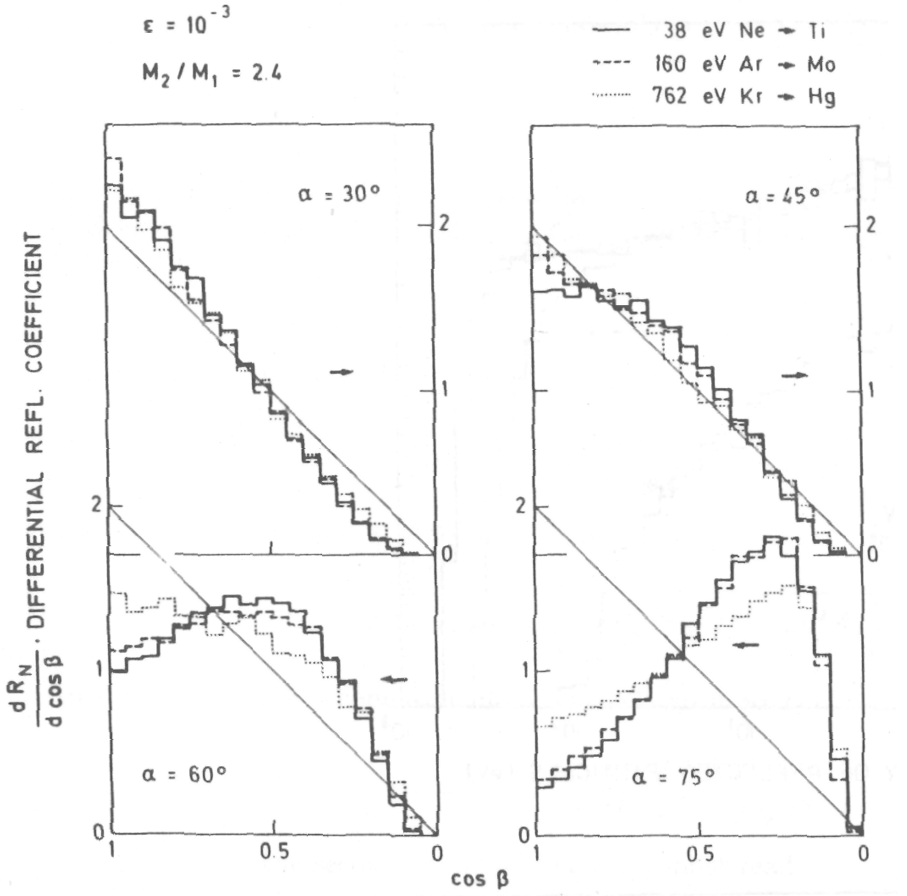

Figure 3.13.: Simulated angular distribution of backscattered particles vs the cosine of the polar emission angle β (integrated over the azimuthal angle φ) for 4 angles of incidence, with a mass ration $M_2/M_1 = 2.4$ and a fixed reduced energy $\epsilon = 10^{-3}$, where $\epsilon = \mu E_0 a/(Z_1 Z_2 e^2)$ with the effective mass μ, the total incident energy E_0, the screening length a and the particle charge numbers Z_1, Z_2.

3.3.2. Analytical model

For the validation of the Monte-Carlo simulation, an analytical model where developed. Here the same strategy were followed as for the simulation. As a result of such an approach one can get the tabulated distribution of the back-scattered particles with respect to the impinging angle. The calculations are done for the infinitesimal approximation. Cylinder symmetry is used to integrate over the azimuthal angle φ.
The chamber consists of two parts: a cylindrical and a spherical one. The split of both parts into relatively small rings, with a height of each ring much smaller, than the chamber dimensions, allows to use infinitesimal approximation. In the following, the cylindrical and the spherical parts are discussed.

3.3.2.1. Cylindrical part

The number of particles emitted in certain direction θ_f can be expressed in such a form (see section 3.3.1):

$$dN_i = \frac{I_i}{q} d\Omega \quad , \tag{3.3.4}$$

where

$$d\Omega = \cos\theta_f d\theta_f d\varphi \quad . \tag{3.3.5}$$

From figure 3.14 it is clear, that $\Delta z_\perp$ can be obtained in two different ways

$$\begin{aligned} \Delta z_\perp &\approx L_i \cdot d\theta_f \quad , \\ \Delta z_\perp &= \Delta z \cdot \cos\theta_f \quad . \end{aligned}$$

The above considerations yield for $d\theta_f$

$$\Delta z \cdot \cos\theta_f = L_i \cdot d\theta \Rightarrow d\theta_f = \frac{\Delta z}{L_i} \cos\theta_f \quad . \tag{3.3.7}$$

The distance between thrsuter exit and intersection point of the particle trajectory with the wall L_i is expressed as:

$$L_i = \frac{R_c}{\cos\theta_f} \quad , \tag{3.3.8}$$

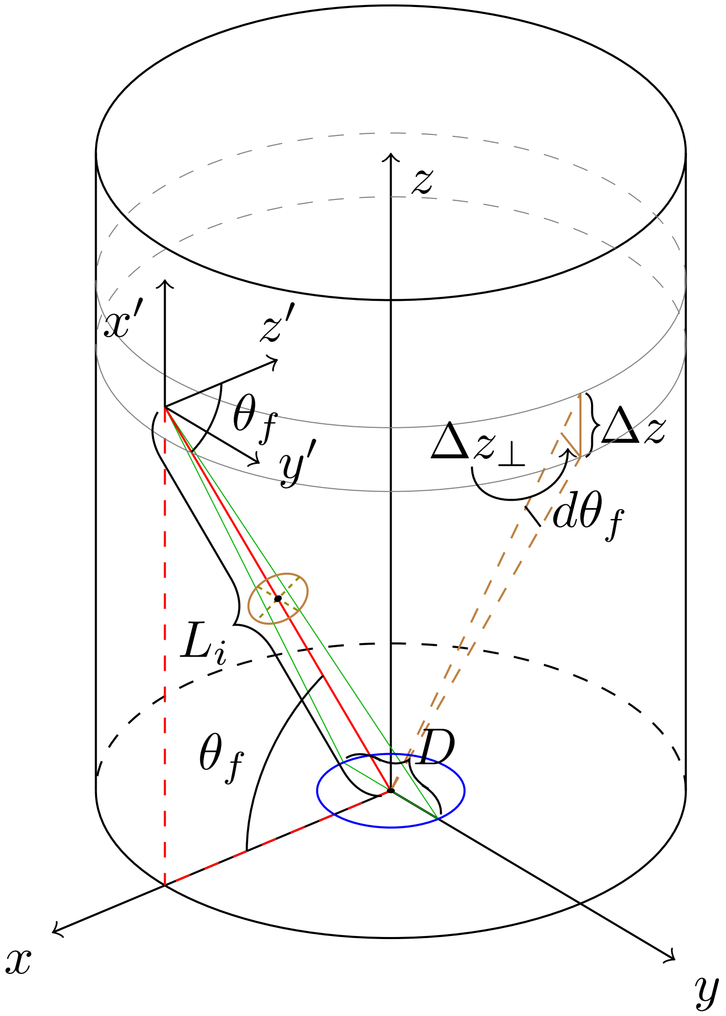

Figure 3.14.: Cylinder

where R_c is the cylinder diameter. Using (3.3.4), (3.3.5), (3.3.7) and (3.3.8) we obtain:

$$dN_i = \frac{I_i}{e} \cos^3 \theta_f \frac{\Delta z}{R_c} d\varphi \quad . \tag{3.3.9}$$

For the carbon flux we get

$$dN_c = \tilde{\mathcal{Y}}(E_i(\theta_f)) f_{re}(\theta_{re}) dN_i d\Omega_{re} \quad , \tag{3.3.10}$$

where the $\tilde{\mathcal{Y}}(E_i(\theta_f))$ is the effective yield dependent on the ion energy, which in turn, relies upon the angle of fall; $f_{re}(\theta_{re})$ is the probability distribution function for the re-emitted particles in the angular direction θ_{re}. Here we take:

$$f_{re}(\theta_{re}) = \frac{\cos\theta_{re}}{\pi} \quad .$$

according to the equation (3.3.3). The effective yield has two components: from Xe^+ and from Xe^{++} and looks like:

$$\tilde{\mathcal{Y}}(E_i(\theta_f)) = (1-\alpha)\mathcal{Y}(E_{Xe^+}) + \alpha\mathcal{Y}(E_{Xe^{++}}) \quad ,$$

where E_{Xe^+} and $E_{Xe^{++}}$ are taken from equations **??**. To collect particles at the same location, emitted ions from, θ_{re} and θ_f are equal (see figurev3.14). The $d\Omega_{re}$ can be obtained from the surface of the ellipse - the projection of the ion thruster in the θ_f direction on the distance of 1 meter depicted by the brown ellipse in figure 3.14 on a plane perpendicular to the L_i segment.
Then the $d\Omega_{re}$ looks like:

$$d\Omega_{re} = \frac{\pi}{4} D^1 D^1_{\perp} \quad , \tag{3.3.11}$$

where D^1 and $D^1_{\perp}$ are the two diameters of the ellipse depicted in figure 3.14 with dashed brown color. The diameters D^1 and $D^1_{\perp}$ can be obtained from the similarity of triangles. For the case of the D^1 the triangles are depicted in the figure 3.14 with green lines and dashed brown line respectively:

$$D^1 = \frac{D}{L_i} \quad , \tag{3.3.12a}$$

$$D^1_{\perp} = \frac{D_{\perp}}{L_i} \quad , \tag{3.3.12b}$$

where

$$D_{\perp} = D\sin\theta_f \tag{3.3.13}$$

is the projection of the diameter D on a plane perpendicular to the plane spanned by L_i and the x axis. Taking into account equations (3.3.11), (3.3.12), (3.3.13) and (3.3.8) one gets:

$$d\Omega_{re} = \frac{\pi}{4}\frac{D^2\sin\theta_f}{R_c^2}\cos^2\theta_f \quad . \tag{3.3.14}$$

Finally, by substituting equations (3.3.14) and (3.3.9) into (3.3.10) we get:

$$dN_c = \frac{\pi}{4}\frac{I_i}{e}\tilde{\mathcal{Y}}(E_i(\theta_f))f_{re}(\theta_f)\sin\theta_f\cos^5\theta_f\frac{D^2\Delta z}{R_c^3}d\varphi \quad .$$

The integration over φ yields:

$$\widetilde{dN_c} = \frac{\pi^2}{2}\frac{I_i}{e}\tilde{\mathcal{Y}}(E_i(\theta_f))f_{re}(\theta_f)\sin\theta_f\cos^5\theta_f\frac{D^2\Delta z}{R_c^3}$$

3.3.2.2. Spherical part

For the case of the sphere, equation (3.3.4) is also valid. In that case, $d\Omega$ will be:

$$d\Omega = \cos\theta_i d\theta_i d\varphi \quad .$$

The unknown $d\theta_i$ is obtained from

$$L_i d\theta_i \approx dl_\perp \quad , \tag{3.3.15}$$

where $dl_\perp$ is the projection of the dl on the L_i. On the Figure 3.15 dl is depicted as brown solid line. Taking into account the following:

$$dl_\perp = dl \cdot \cos\theta_{re} \quad , \tag{3.3.16a}$$

$$\theta_{re} = \theta_p - \theta_i \quad , \tag{3.3.16b}$$

$$dl \approx R_{sp}\Delta\theta_p \quad , \tag{3.3.16c}$$

where R_{sp} is the sphere radius, and substituting (3.3.16) into (3.3.15) we have:

$$d\theta_i = \frac{R_{sp}\cdot\cos(\theta_p - \theta_i)\Delta\theta_p}{L_i}$$

and thus

$$dN_i = \frac{I_i}{e}\sin\theta_i\frac{\cos(\theta_p - \theta_i)}{L_i}R_{sp}\Delta\theta d\varphi \quad . \tag{3.3.17}$$

For the re-emission as a starting point we use again (3.3.10). Using similar considerations as for the cylindrical case we get $d\Omega_{re}$ as:

$$d\Omega_{re} = \frac{\pi}{4}\left(\frac{D}{L_i}\right)^2\cos\theta_i \tag{3.3.18}$$

Combining (3.3.17), (3.3.18) into (3.3.10) gives

$$dN_c = \frac{\pi}{4}\mathcal{F}(\theta_p, \theta_i)\frac{R_{sp}}{L_i}\left(\frac{D}{L_i}\right)^2 \cos\theta_i \cdot \sin\theta_i \cdot \cos(\theta_p - \theta_i)\Delta\theta_p d\varphi \quad .$$

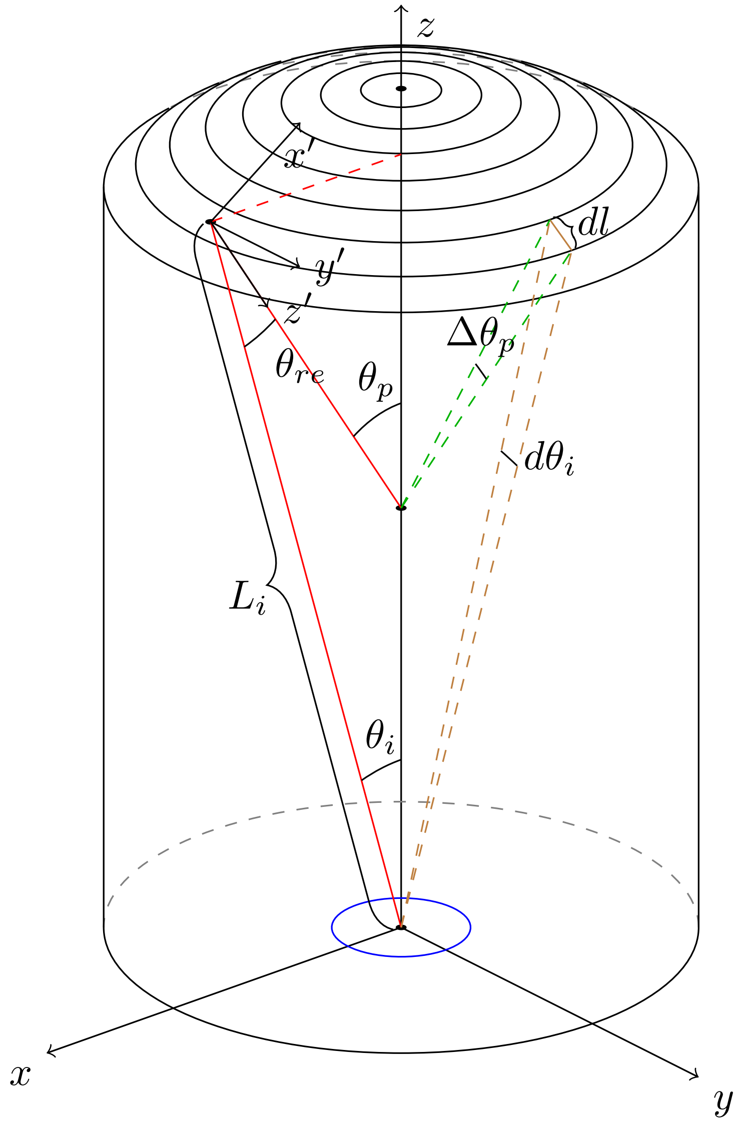

Figure 3.15.: Spherical case

After integration we finally get:

$$\widetilde{dN_c} = \frac{\pi^2}{2}\mathcal{F}(\theta_p,\theta_i)\frac{R_{sp}}{L_i}\left(\frac{D}{L_i}\right)^2 \cos\theta_i \cdot \sin\theta_i \cdot \cos(\theta_p - \theta_i)\Delta\theta_p \quad ,$$

where $\mathcal{F}(\theta_p,\theta_i)$ is expressed as:

$$\mathcal{F}(\theta_p,\theta_i) = \frac{I_i}{e}\tilde{\mathcal{Y}}(E_i(\theta_i))f_{re}(\theta_p - \theta_i) \quad .$$

3.3.3. Results

The calculated angular distribution of the back scattered particles by the Monte-Carlo simulation and from the analytical model are shown in figure 3.16. Due to the larger intersection of the solid angle with the thruster exit plane, the particle flux is larger for small angles of incidence. One can also see that the returned particle flux consists of two parts, due to the vessel geometry. Sputtered particles from the spherical end are giving the contribution of small angles between 0 and 15 degrees, while for larger angles the sputtered particles are from the cylinder walls. One can see, that the Monte-Carlo simulation (full line) agrees to the analytical calculations (dashed lines).

In further simulations these results can be used to verify structure of co-

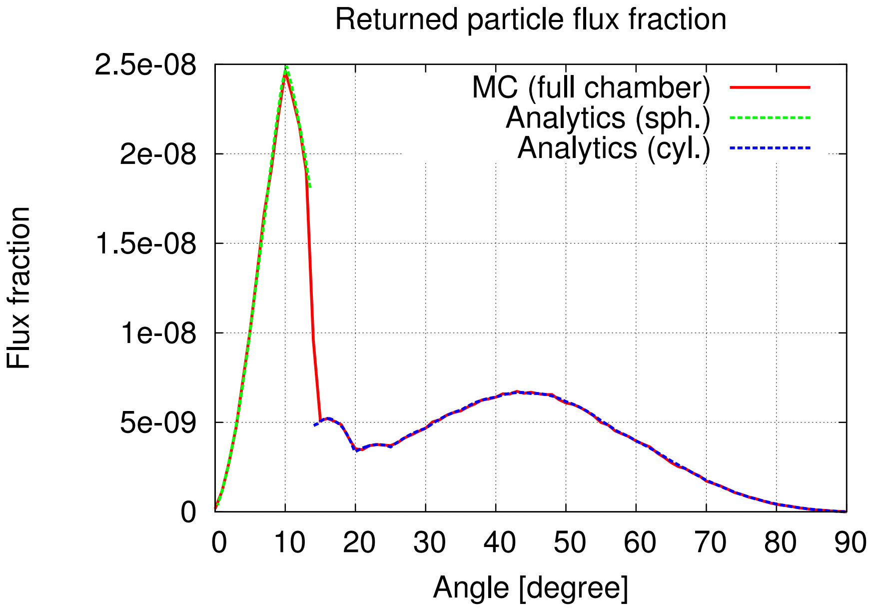

Figure 3.16.: Returned particle flux.

deposited layers inside the thruster channel and its impact on the measured thrust.
The advantage of the shown simulation is its flexibility to analyze on different vessel geometries. Also the analytical mode, which is used here as a validation, can be used to calculate the distribution of the back scattered particles. It needs a much smaller numerical effort than the Monte-Carlo simulation, but it can not be applied to other geometries as easy as the other one.

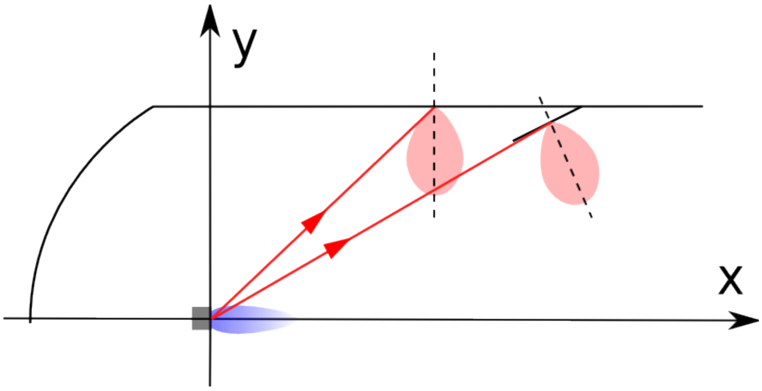

Figure 3.17.: Effect of a baffle on the distribution of sputtered particles.

In spite of the low back flowing fraction of emitted particles ($< 1\%$), this particles are producing co-deposited layers during the long test runs. These layers are causing artifacts in the thrust. A strategy for avoiding this is to implement baffles in the vessel. While the $cos(\theta)$ distribution of the sputtered particles do not depend on the angle of incidence of the impinging ion, theses tilted baffles are turning the direction of the distribution and reducing the back-flow to the thruster exit, as sketched in figure 3.17. With that sketch it is clear that a tilting of the baffles in the other direction would increase the particle back-flow. A implementation of those baffles in the whole vessel, as sketched in figure 3.18

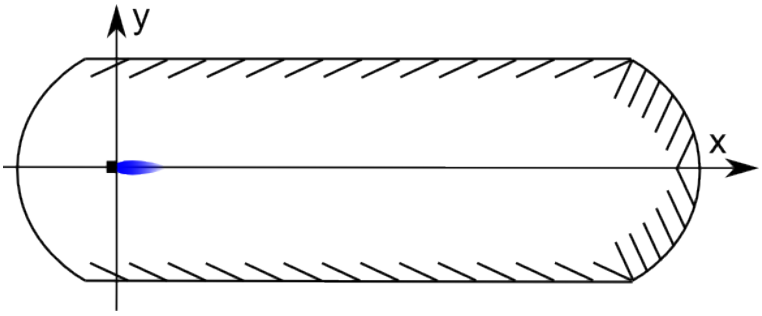

Figure 3.18.: Sketch of a vacuum vessel with implemented baffles.

reduces the back flow by $40\% - 66\%$. As a result of this analysis, the company Aerospazio implements baffles tilted by about $20°$ to reduce artifacts due to sputterd particles from the vessel walls.

4. Plasma instabilities in the thruster channel

In the last chapter the different operational plasma characteristics for the SPT and the HEMP thruster were discussed. It was shown, that for the SPT, plasma-wall interaction takes place in the whole channel. In the HEMP thruster the main contribution of plasma-wall interactions is limited only to the cusp regions.

As mentioned in equation 2.3.1, the current density at the walls depends exponentially on the potential drop $\Delta\phi$. Nonlinear dependencies in systems always create waves and turbulence. A simple example is a periodically driven pendulum, which shows chaotic behavior for particular angular frequencies. For bounded plasmas, sheath instabilities can trigger instabilities in the plasma volume, leading to an anomalous diffusion of plasma particles.

In the discussed ion thrusters, anomalous diffusion is observed for electrons. Both thrusters need electrons inside the thruster channel to ionize the propellant gas. Because of the position of the primary source, without anomalous transport electrons would mostly enter the thruster channel near the thruster walls. For electrons entering the thruster channel near to the axis, either classical diffusion due to collisions or anomalous transport due to turbulences, is needed. Inside the thruster channel, the anomalous diffusion builds up the distribution of the electrons density. In the SPT channel, magnetic field lines are perpendicular to the walls, a transport of electrons towards the anode can be produced only by classical collisional diffusion and anomalous diffusion. In the HEMP thruster magnetic field lines near the axis are mainly parallel to the channel walls and give a straight connection between channel exit and anode. Therefore, electrons which enter the thruster channel near to the channel axis, are directly attracted by the anode potential. But if electrons are following the magnetic field lines close to the channel wall, they get trapped by the first cusp, the exit cusp. To fill the inner anode cusp, diffusion from the exit cusp is needed. But in contrast to the SPT only small distances must be crossed. The electrons in the magnetic bottle formed by two subsequent cusp are following magnetic field lines parallel to the walls.

4.1. Anomalous diffusion of electrons

In many experiments anomalous diffusion of electrons across magnetic field lines are observed, for example in the SPT, where it results in erosion of the thruster channel wall, which is much higher than expected from classical estimates.
The first considered source of this process was the collision of electrons with other plasma particles, the so called classical diffusion. In plasmas of the here discussed ion thrusters, large neutral densities are existing, therefore electron-neutral collisions are dominant. In the presence of a magnetic field, they can be seen as collisions of the guiding center of the gyrating electron with the neutral. In statistical diffusion, the diffusion coefficient D is proportional to the mean free path λ_{mfp} and the average time τ between two collisions

$$D \quad \propto \quad \frac{\lambda_{mfp}^2}{\tau} \quad . \tag{4.1.1}$$

Due to the gyration of the electrons, the mean free path in a plasma with an external magnetic field is its Larmor radius $r_{L,e} = \frac{|\vec{v}_{\perp,e}|}{\omega_{c,e}}$. For a strong magnetic field with $\omega_{c,e}\tau >> 1$, the diffusion coefficient due to neutral scattering is given in [18] as

$$D_\perp \quad = \quad \frac{k_B T_e}{m_e \tau \omega_{c,e}} \propto \frac{\vec{v}_{th,e}^2}{v_{\perp,e}^2} \frac{r_{L,e}^2}{\tau} \propto \frac{1}{B^2} \quad . \tag{4.1.2}$$

While the Larmor radius is proportional to $1/B$, the diffusion across the magnetic field scales with $1/B^2$. While for diffusion along magnetic field lines collisions are decreasing the mean free path and therefor the collision coefficient, here collisions are necessary, therefore $D_\perp$ is proportional to the collision frequency $\nu = 1/\tau$. But in the measured transport, the contribution of classical diffusion is not sufficient to explain the experimental observations [19].
Another kind of diffusion was introduced in 1946, the so called "anomalous diffusion". While in almost all experiments $D_\perp$ scales with B^{-1} rather than with B^{-2}, a semi empirical formula was noted by D. Bohm, E. Burhop, and H. Massey, with a diffusion coefficient [18]:

$$D_\perp \quad = \quad \frac{1}{16} \frac{k_B T_e}{eB} = D_B \quad . \tag{4.1.3}$$

A general derivation for $D_\perp \propto B^{-1}$ was given by L. Spitzer in 1960 [20], with

$$D_\perp \quad = \quad 2(K_1 K_2)^2 K_3 \cdot \frac{k_B T_e}{eB} \quad . \tag{4.1.4}$$

K_1, K_2, K_3 are empirical constants, determining the strength of the electron perturbation perpendicular to the magnetic field.

Nowadays three sources for anomalous diffusion are accepted [6]:
1) gradient induced transport
Due to density and field gradients of small length scales, non-local effects are appearing. They are leading to a distortion of the particle gyro-motion. This effect is known as "neo classical conductivity" and can be influenced by the wall material.
2) wall induced transport
Due to electron-wall interaction, like SEE or non-ideal reflecting walls, transport is induced. Also other mechanism like micro roughness of the surface, ion-wall recombination, photo-electron emission from the wall due to UV radiation or sheath oscillation take part in the anomalous diffusion.
3) fluctuation of the electric field component perpendicular to the wall
This fluctuation, which can also be written as a Fourier series $|E_k| exp\{-i\varphi_k(t)\}$, can appear in two different ways. Either the phases $\varphi_k(t)$ are statistically distributed in time or they are given by coherent waves $\varphi_k(t) = -\omega t + k_l r_l$, where the index l denotes the direction perpendicular to the wall. In the first case the anomalous diffusion depends on the correlation time of the electric field, whereas resonance of particles and waves is the leading factor for the anomalous diffusion due the superposition of coherent waves. The most probable origins of these types of electric field fluctuation can be micro-instabilities, resistive instabilities, gradient driven instabilities perpendicular to the wall or electron driven instabilities.
In section 4.3, it will be shown for ion thrusters, that an instability in the resistivity, induced by an instable plasma sheath due to strong SEE, leads to a fluctuation of the electric field, perpendicular to the plasma limiting wall. In section 4.4, a self-consistent simulation of a HEMP thruster model will show that electrostatic turbulences appears also for studies without SEE.

4.2. Plasma sheath with a strong electron emitting wall

As described in section 2.3, secondary electron emission decreases the potential drop at the wall, to prevent a net flow current. The effective potential drop is given with

$$e\Delta\phi^{eff} = -k_B T_e \ln\left[(1-\gamma)\sqrt{\frac{m_i}{2\pi m_e}}\right]$$

[4] and decreases with an increasing secondary electron emission coefficient γ. If γ approaches unity, that approximation brakes down. But before this point is reached however a new physical phenomena becomes important. One can show that for a critical emission coefficient γ_c, the electric field at the wall gets zero. For $\gamma > \gamma_c$ no monotonic solution for $\phi(x)$ exists. In order to reach a stable situation, a potential wall forms, so that a fraction of the emitted electrons are returning to the wall and the effective emission coefficient decreases to $\gamma \equiv \gamma_c$. In this regime, the current density of the emitted secondary electrons at the wall is limited by the space charge in front of the wall.
For the calculation of γ_c, we consider a plasma, bounded by a conductive wall at $x = 0$, where the x-coordinate determines the direction perpendicular to the wall and $x = \infty$ the plasma bulk. The plasma potential is set as zero $\phi(\infty) = 0$. While the plasma sheath is determined by the Poisson equation, one has to find expressions for the particle densities. For Maxwellian distributed electrons, the electron density without the secondary electrons is given by the difference of the plasma density n_0 and the density of the secondary electrons in the plasma bulk $n_{e,s}(\infty)$, affected by the wall induced potential $\phi(x)$.

$$n_{e,p}(x) = [n_0 - n_{e,s}(\infty)]\, exp\left\{e\phi(x)/k_B T_e\right\} \tag{4.2.1}$$

While the electrons are pushed off by the wall potential, the ions are attracted and their density can be written as

$$n_i(x) = n_0 \left(\frac{E}{E - e\phi(x)}\right) \quad , \tag{4.2.2}$$

where $E = m_i v_i^2/2$ is the ion energy. From the continuity equation $n_{e,s} v_{e,s} = \gamma/(1-\gamma) n_0 v_0$ one get with $v_{e,s} = \sqrt{2e(\phi - \phi_0)/m_e}$ the density for the secondary electrons

$$n_{e,s}(x) = n_0 \frac{\gamma}{1-\gamma} \left(\frac{m_e}{m_i} \frac{E}{e(\phi(x) - \phi_0)}\right)^{1/2} \quad , \tag{4.2.3}$$

where $\phi_0 = \phi(x = 0)$ is the wall potential. The one dimensional Poisson equation $\frac{\mathrm{d}^2\phi}{\mathrm{d}x^2} = 4\pi\left(n_{e,p} + n_{e,s} - n_i\right)$ gives with equation 4.2.1 - 4.2.3 and one integration over x, the following expression:

$$\begin{aligned} \frac{1}{8\pi n_0 k_B t_e}\left(\frac{\mathrm{d}\phi}{\mathrm{d}x}\right)^2 &= \frac{2E}{k_B T_e}\left[\sqrt{1 - \frac{e\phi}{E}} - 1\right] + \frac{2\gamma}{1-\gamma}\sqrt{-\frac{m_e E e\phi}{m_i k_B^2 T_e^2}} \\ &\times \left[\left(\sqrt{1 - \frac{\phi}{\phi_0}} - 1\right) + \left(1 - \frac{\gamma}{1-\gamma}\sqrt{-\frac{m_e E}{m_i e \phi_0}}\right)\right] \end{aligned}$$

$$\times \quad \left(exp\left\{ \frac{e\phi}{k_B T_e} \right\} - 1 \right) \quad .$$

Due to the squared factor of the potential derivative, also the right hand side has to be larger than zero, for all $\phi = \phi(x)$. That leads to the following expression for the ion energy [4]

$$E \;=\; \frac{k_B T_e}{2} + \frac{\gamma}{1-\gamma} \left(\frac{m_e}{m_i} \right)^{1/2} \left(-\frac{E}{e\phi_0} \right)^{3/2} \left(\frac{k_B T_e}{2} - e\phi_0 \right) \quad . \tag{4.2.4}$$

If we consider that the total current density is zero in steady-state, we get

$$\begin{aligned} j_i \;&=\; j_{e,p} - j_{e,s} \\ \frac{\gamma}{1-\gamma}\sqrt{\frac{2E}{m_i}} \;&=\; \frac{1}{4}\left[1 - \frac{\gamma}{1-\gamma}\sqrt{-\frac{m_e E}{m_i e\phi_0}} \right] exp\left\{ \frac{e\phi_0}{k_B T_e} \right\} \sqrt{\frac{8 k_B T_e}{\pi m_e}} \end{aligned} \tag{4.2.5}$$

If one eliminates $\frac{1}{\gamma - 1}$ between the equation for the zero net current at the wall (4.2.5) and the ion energy at the sheath entrance (4.2.4), one gets for a static wall potential $\left(\frac{\mathrm{d}\phi}{\mathrm{d}x}\right)_0 = 0$ and the previous singularity $\gamma = 1$, the critical values of the sheath potential and the ion energy at the sheath entrance:

$$\begin{aligned} e\phi_{0,c} \;&=\; -1.2 \cdot k_B T_e \\ E_{i,c} \;&=\; 0.58 \cdot k_B T_e \end{aligned}$$

Substituting both expressions in the zero net current condition at the wall (4.2.5), one gets the critical value for the secondary electron emission coefficient between a stable and an unstable sheath

$$\gamma_c = 1 - 8.3\sqrt{\frac{m_e}{m_i}}$$

For an argon plasma the critical emission coefficient is $\gamma_c = 0.95$.
This theory is based on the assumption that the zero total current density at the wall is given in steady-state:

$$j_i = j_{e,tot} \quad \Longleftrightarrow \quad I_i = -I_{e,tot} \quad ,$$

where the total current $I_{e,tot} = I_{e,p} - I_{e,s} = I_{e,p}(1-\gamma)$. The negative sign of the secondary electron current is due to the flight direction away from the wall. For a SEE with $\gamma < 1$, the potential drop at the wall decreases, if I_i increases. That means the sheath voltage $V = \phi_0$ decreases in order to enhance the primary electron flow $I_{e,p}$, the sheath will reach a state of equilibrium. But if γ exceeds 1, a negative differential resistance at the wall $(\partial I/\partial V)^{-1} < 0$ can appear. If I_i increases in this case, then the voltage sheath drop cannot decrease because otherwise the primary electrons would strike the wall with higher energy and create a higher emission current of secondary electrons $I_{e,s}$. That would increase the positive current [21]. The phases of negative and positive differential resistance result into a strong random noise in the electron density in front of the wall. That intermittency causes a non-Gaussian electron velocity, the sheath loses its static character and gets an oscillating structure, the so-called sheath instability.

Another possible explanation of this instability can be given by the beam-plasma instability [22]. Here the stream of particles from the wall moving through the plasma causes a plasma density perturbation which is proportional to the beam density.

4.3. Connection of sheath instability and bulk plasma

After the investigation of the sheath instability in one dimension, one likes to know, how the spatial structure of such instabilities affects the whole plasma. As a first step, a PIC simulation are done in 2D (r, θ).

As described in the last section, the instable plasma sheath is caused by a temporary negative differential resistance. Due to the fluctuating radial sheath potential, the radial drift energy jumps. This jump triggers an azimuthal electric field fluctuations ∂E_θ dependent on the frequency of the sheath instability.

In [21] the connection between the sheath instability and ∂E_θ is shown for SPT. For electron energies of $15 - 20eV$, which is needed for ionization, the wall material gets a secondary emission coefficient larger than the critical value, which leads to instabilities in the sheath potential. Due to the radial geometry of the SPT, the ion flux onto the inner wall is higher than onto the outer wall, so that a stronger SEE appears at the inner wall. The electron emitting wall can be seen as an electron beam pointing inside the plasma. That causes an instability in the plasma bulk. With a (r, θ) PIC simulation, a instabilities in the azimuthal distribution of the plasma potential were found, as can be seen in figure 4.1 left. It can be seen, that the potential propagates like a wave in the direction of θ with a nearly constant wave number. The time evolution of this potential profile (4.1 right) shows, that after an initial time of development, the potential wave is propagating with an approximately constant velocity. The high amplitude at the beginning is due to a transient effect.

The fluctuation ∂E_θ modulates the electron azimuthal beam, which causes

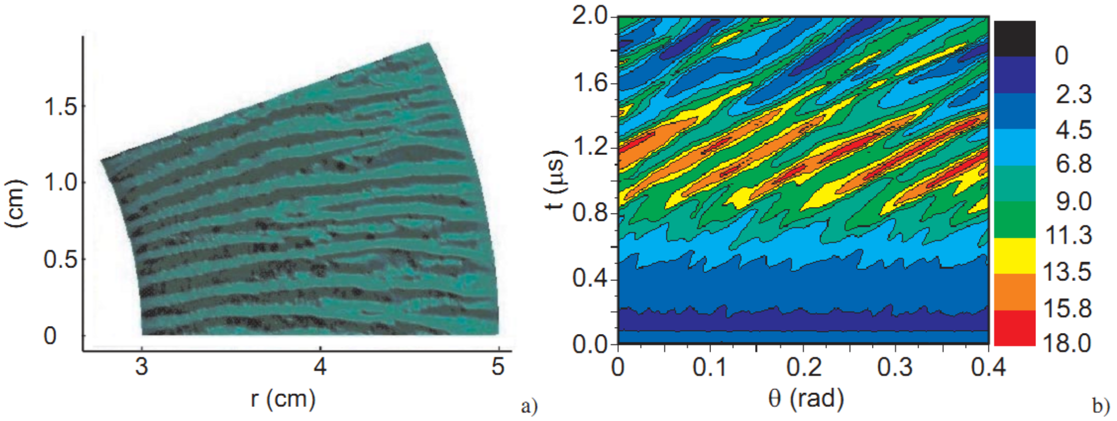

Figure 4.1.: a) Distribution of plasma potential in the r, θ plane. b) Time evolution of the azimuthal profile of plasma potential (in V) calculated at $r = 4cm$. Here SEE where implemented only at the outer wall. From [6]

charge imbalance. That means, the azimuthal field oscillation gives an axial kick to the charged plasma particles. This corresponds to the motion of a linear oscillator in a traveling wave field, known as kicked rotor [23]. For the electrons, following the magnetic field perpendicular to the wall, this kick produces a transport across the magnetic field lines. A resulting axial drift towards the anode from such a fixed oscillating azimuthal potential were calculated in a 2D (θ, z) PIC simulation of the SPT in the work of [21].
While both simulations are two dimensional in space and three dimensional in velocity space, the anomalous transport of the electrons inside the thruster channel was realized by a Bohm diffusion, with the semi empirical diffusion coefficient D_B. Depending on the electric field, the particle gets an additional velocity towards the anode. A self-consistent 3D PIC simulation of a simplified HEMP model is prescribed in the following chapter, allowing to validate the chosen turbulence model in 2D.

4.4. A self-consistent simulation of the HEMP thruster

For a self-consistent simulation of anomalous transport in ion thrusters, a three dimensional plasma simulation is needed. For PIC, an increase of dimension needs additional numerical requirements, which will be described in the next section. Afterwards results of a 3D PIC simulation for the HEMP thruster is shown.

4.4.1. A Parallel Poisson solver for a 3D electrostatic PIC simulation

For large plasma systems, it is useful to parallelize the calculation for particle pusher and the Poisson equations in the PIC code. For the particle mover the division of the simulation domain in sub domains make it easy to calculate the equation of motion on different cores. For the solver, the back-solve of the Poisson equation has to be divided. That can be done with the commonly used program package SuperLU_Dist. As described in a section 2.4.2 the Poisson equation can be approximated by a matrix equation with a matrix of constant entries. Therefore the factorization has to be calculated only once, while the back-solve has to be solved in every PIC cycle. The calculation time for a back-solve depends on the ratio between the non-zero entries and the zero entries of the matrix, the sparsity. For the same sparsity, the time for one back-solve in general matrix solvers depends linearly on the matrix size. But for an increase of a grid dimension, also the Poisson equation increases in dimension and its discretization lead to more bands and boundary conditions therefore less sparsity. The linear dependence is not granted anymore. To verify the calculation for one back solve, numerical measurements were done for different sizes of domain grids. An ideal solver for a PIC simulation would need a back solving time of $\tau < 1s$ to prevent extra large calculation time and would get faster with a larger amount of parallel processes. To simulate the thruster channel of HEMP ($R = 9mm,\ L_z = 43mm$), a minimum grid of $49 \times 49 \times 118$ grid cells is needed. With an additional plume region a minimum grid of $132 \times 132 \times 245$ cells is needed.
For a three dimensional grid, the Poisson equation is given as

$$-\nabla^2 \phi(\vec{X}_j) = \frac{1}{\epsilon_0} \rho(\vec{X}_j)$$

and had to be solved for every grid point $\vec{X}_j$ for $j = 1, ..., (N_{gx} + 1) \cdot (N_{gy} + 1) \cdot (N_{gz} + 1)$ of the $N_{gx} \times N_{gx} \times N_{gz}$ sized grid. With the notation $\phi(\vec{X}_j) \equiv \phi_{i,j,k}$, where the index i gives the x-component, j the y-component and k the z-component of the location $\vec{X}_j$ in space, the discretization of the second derivative, as described in chapter 2.4.2 gives for a homogeneous grid $\Delta x \equiv \Delta y \equiv \Delta z$

$$\nabla^2 \phi_{i,j,k} = \frac{\phi_{i+1,j,k} + \phi_{i,j+1,k} + \phi_{i,j,k+1} - 6\phi_{i,j,k} + \phi_{i-1,j,k} + \phi_{i,j-1,k} + \phi_{i,j,k-1}}{\Delta x^6} \tag{4.4.1}$$

In our PIC simulation the values of $\phi_{i,j,k}$ and $\vec{\rho}' := \frac{-\Delta x^6}{\epsilon_0}\vec{\rho}$ are saved in one dimensional arrays, with $\varphi_l = \phi(i + (j \cdot N_y) + (k \cdot N_y \cdot N_z))$ and $\varsigma_l = \rho'(i + (j \cdot N_y) + (k \cdot N_y \cdot N_z))$. That transforms equation 4.4.1 to a matrix equation $\hat{\mathrm{A}}\vec{\varphi} = \vec{\varsigma}$, where $\hat{\mathrm{A}}$ is a 7 band matrix with constant entries. It is a quadratic matrix and has in principle $(N_{gx} + 1)^2 \cdot (N_{gy} + 1)^2 \cdot (N_{gz} + 1)^2$ entries. While for three dimensional simulations also the particle mover is parallelized, additional grid cells are added, to prevent numerical artifacts. But this increases the matrix size only slightly. The storage format, SuperLU deals with is the compressed column format, also known as "Harwell-Boeing format" [9]. It saves the matrix entry and its position in the matrix, which is saving storage for sparse matrices, like $\hat{\mathrm{A}}$.

In the parallel version, SuperLU_Dist, the matrix factorization and solving is done in parallel on different cores. Therefore matrix $\hat{\mathrm{A}}$ and vector of density $\vec{\varsigma}$ are distributed among all the processes. They use the same distribution based on block rows. That is, each process owns a block of consecutive rows of $\hat{\mathrm{A}}$ and $\vec{\varsigma}$. Each local part of the sparse matrix is stored in the Harwell-Boeing format. The factorization $\hat{\mathrm{A}} = \hat{\mathrm{L}}\hat{\mathrm{U}}$ on these cores, and the calculation of $\hat{\mathrm{L}}^{-1}$ and $\hat{\mathrm{U}}^{-1}$ is done in PIC only once at the beginning of the simulation. For the back-solve, which takes place at every PIC step, each core calculates with its sub-matrices and the whole array $\vec{\varsigma}$ a part of the potential array $\vec{\varphi}$, with $\vec{\varphi} = \hat{\mathrm{L}}^{-1}\hat{\mathrm{U}}^{-1}\vec{\varsigma}$. After the back-solve, the solution is put together on the core, where SuperLU_Dist is running. More details can be found in the manual of the SuperLU package [**?**].

For the testing of the average time for one back-solve of a large matrix, calculation of the above described matrix $\hat{\mathrm{A}}$ was made on a computer cluster, provided by the Max Planck Institute of Plasma Physics (IPP) in Greifswald. In figure 4.2 - 4.4 the calculation time for the matrix factorization (left) and the back-solve dependent on the number of used processors, for different grid sizes are shown. The time for one back-solve is averaged over 200 samples and the root mean square deviation is shown as error bars. If available, the calculation time of the serial SuperLU program was added (crosses) in the plots.

For a small grid with of $L_x = 20,\ L_y = 20,\ L_z = 20$ grid cells, the matrix has $(20 + 1)^6 \approx 10^8$ entries. Additional grid cells due to a parallel mover were not taken into account. One can see that for a number of processor > 5, the time for one back-solve is varying between $0.1s$ and $0.25s$. That is due to the communication between processors, to provide the parts of the matrices. For a smaller number the time for one back-solve is $\tau \approx 0.02s$. One can see that τ is slightly decreasing, so that for a matrix with this size the ideal number of processors for the SuperLU_Dist program is 4. But compared with the serial version, as shown as crosses, SuperLU_Dist is slightly slower. Also for the factorization time the serial solver calculates faster than the parallel one with one processor, but for 4 processeors the time for the matrix factorization can be decreased to $0.8s$.

For a grid of $50 \times 50 \times 50$ grid cells, $\hat{\mathrm{A}}$ has $(50 + 1)^6 \approx 10^{10}$ entries. For

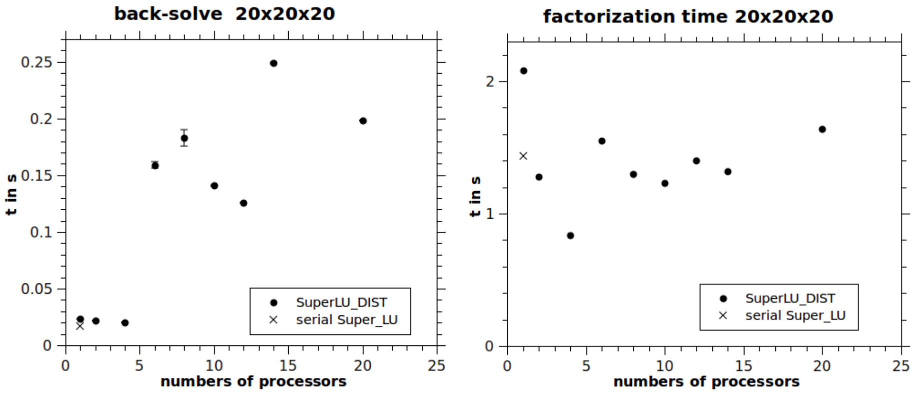

Figure 4.2.: Calculation time of the matrix solver program SuperLU_Dist. Factorization time (left) and back-solve time (right) of a Poisson matrix for a grid of $20 \times 20 \times 20$ grid cells.

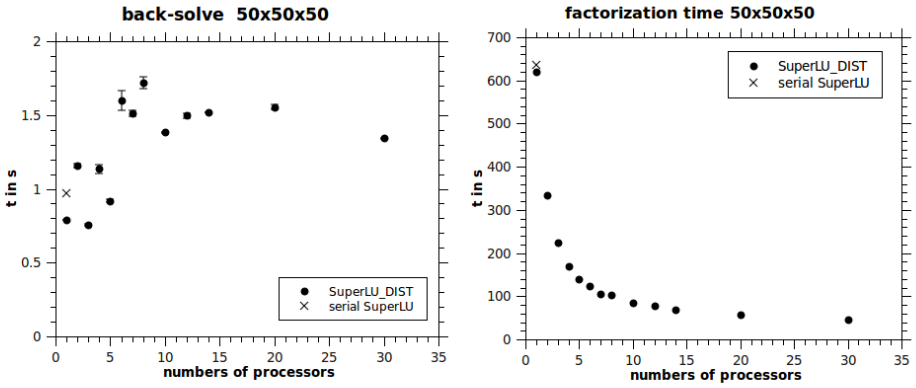

Figure 4.3.: Calculation time of the matrix solver program SuperLU_Dist. Factorization time (left) and back-solve time (right) of a Poisson matrix for a grid of $50 \times 50 \times 50$ grid cells.

that matrix size, communication between the processors to provide the parts of the matrix, is dominating, while the back-solve time is not decreasing with the number of processors. One can see in figure 4.3, that for 1-12 processors τ is increasing due to the large size of the partial matrices, yielding a lot of communication between the processors. For numbers larger than 12, τ is decreasing, due to the smaller size. Contrary to that the factorization time is decreasing with the number of processors, so that the SuperLU_Dist needs only $50s$, if it operates with 30 processors, instead of $640s$ with the serial SuperLU.

For a large matrix, representing a grid with $100 \times 100 \times 100$ grid cells, $\hat{A}$ has $(100+1)^6 \approx 10^{12}$ entries. In figure 4.4 a decrease of back-solve time and factorization time with an increasing number of processors is observed. For one

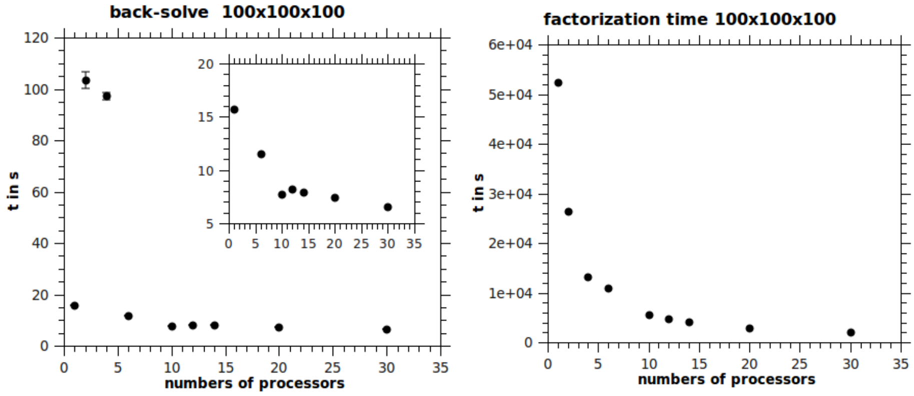

Figure 4.4.: Calculation time of the matrix solver program SuperLU_Dist. Factorization time (left) and back-solve time (right) of a Poisson matrix for a grid of 100 × 100 × 100 grid cells.

processor, no communication between processors is needed, therefore τ is very low. The high values for 2 and 4 processors are due to the large sub-matrices, which causes much communication time. A computer cluster with better communication would decrease this effect. The time for one back-solve of a matrix of this size is decreasing with the number of processors, but always takes more than $5s$.
For a PIC simulation of the thruster channel of HEMP, the solve of the Poisson equation, with a grid size of $50 \times 50 \times 100$, SuperLU_Dist has a longer calculation time than SuperLU. Also for a larger grid, which is needed to simulate the channel and the plume region, a calculation time larger than $5s$ is too much for one back-solve, while the solution of the Poisson equation has to be repeated about $N_{PIC} = 10^5$ times for one PIC simulation. The matrix solver SuperLU_Dist is too costly for a 3 dimensional PIC simulation and is therefore not used in the self-consistent simulation of the HEMP thruster.

4.4.2. Results

To study anomalous diffusion in the HEMP thruster, a three dimensional simulation with an electrostatic PIC code is calculated. For a 3-dimensional analysis of the influence of plasma-wall interactions on the plasma potential, a 3D simulation of an idealized HEMP thruster was done. The program, which was used, was written by Konstantin Matyash [24].
Because the calculation is very costly, only proof of principle for studying anomalous transport in a HEMP-like geometry was possible. The HEMP thruster has a

cylindrical volume. But in a PIC simulation a cylindrical grid causes self forces. To avoid that, a Cartesian grid is chosen. The HEMP model is set up as a cuboid, based on a Cartesian grid. To be able to obtain a solution in a reasonable run time (one week), the size of the system is scaled down by factor of 50. In order to preserve the ratio of the charged particles mean free paths and the gyroradii to the system length, the neutral Xenon density and the magnetic field are increased by the same factor 50 [**?**].

The simulation domain has a height and width of $L_x = L_y = 23mm$, a length of $L_z = 130mm$ and includes the thruster channel as well as the plume region, as shown in sketch 4.5. The thruster exit is positioned at $z = 51mm$ and the two cusps at $z = 20.5mm$ (anode cusp) and $z = 37mm$ (exit cusp). The channel walls consist of boron nitride layers, which are $1.5mm$ thick. The external domain boundaries consist of metal walls with a potential of $\phi = 0$. The anode voltage, applied at $z = 0mm$ is set to $500V$. Particles which are hitting the metal as well as the dielectric boundaries are absorbed. In the thruster channel, these particles are contributing to the local surface charge. To identify anomalous diffusion driven by turbulence, no SEE was run.

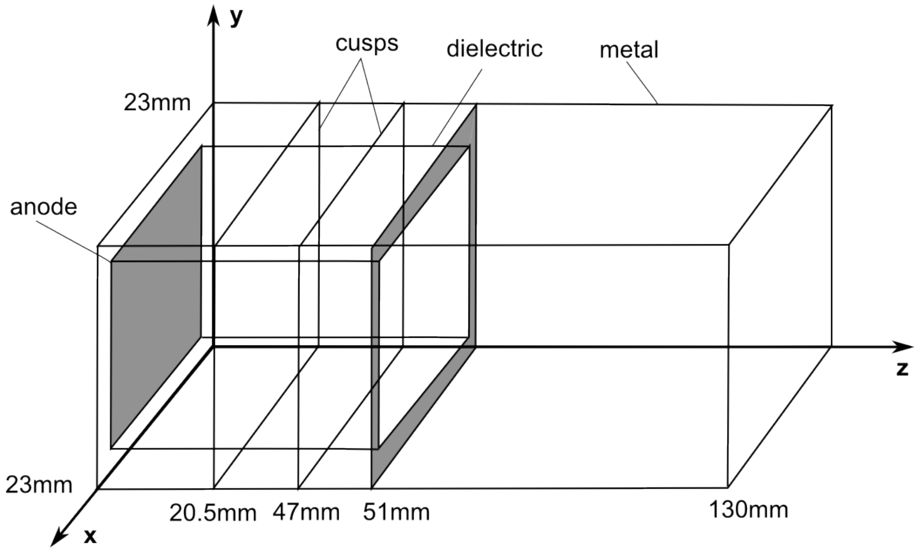

Figure 4.5.: Schematic view of the computational domain for a HEMP-like thruster model.

For the 3D PIC program, particle mover, field weighting and collisions are implemented as described in the one-dimensional case. Based on the results presented before, the solver is not parallelized and after the LU decomposition the back-solve is computed on one processor. For the neutral argon atoms, the density profile was prescribed by an exponential profile $n_n = n_n exp\{-Z/L\}$, with $L = Z_{max}/2.5$ and $Z_{max} = 65mm$. Such density profile is close to the one obtained from self consistent models in 2D.

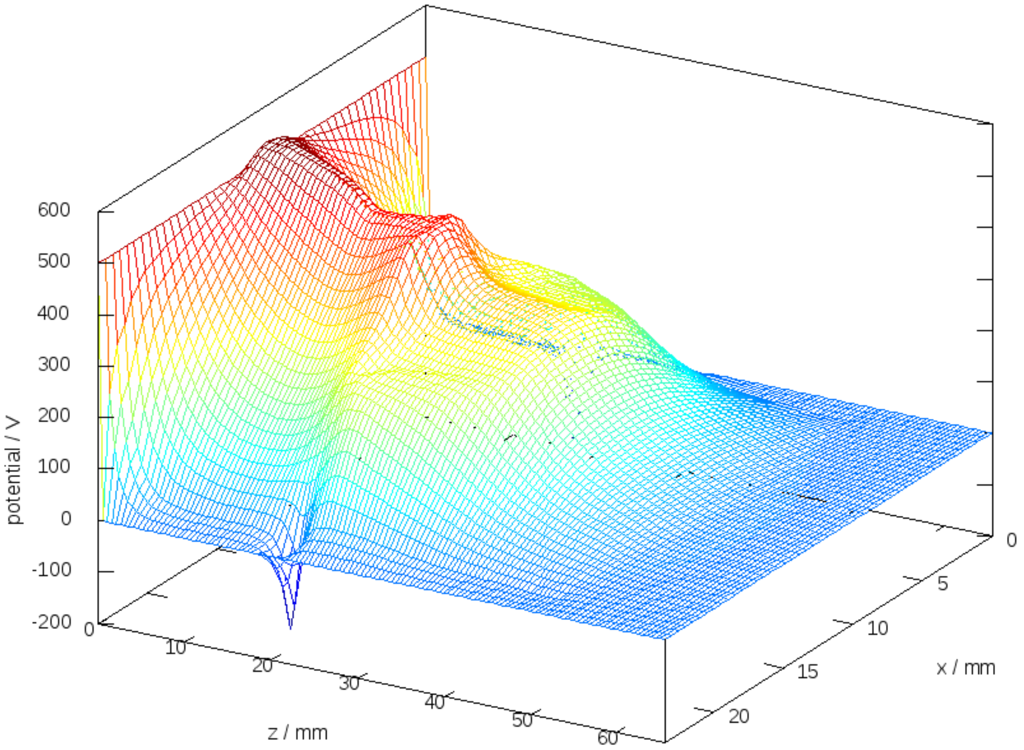

Figure 4.6.: Plasma potential along the y-axis of a HEMP thruster model at $y = 15.5mm$.

In the following, the three dimensional data is shown in two dimensional cuts. In figure 4.6 a profile of the plasma potential along the y-axis, for $y = L_y/2$, is shown. One can see that the potential has a step like shape in the z-direction, which is caused by the two cusps. Behind the thruster exit, the potential drops from $200V$ to $0V$. The potential shape is in good agreement with the 2D results, as shown in figure 3.5. Slight differences are due to different operational parameters.

At $z = 20.5mm$, the potential gets negative at the wall. This is the anode cusp region, where the magnetic field lines are perpendicular to the wall. The second cusp region can be identified by a potential plateau in the magnetic bottle between $z = 23 - 37mm$.

In figure 4.7 the potential in this cusp is shown in the x-y-plane. One can see, that the variation of the potential is not purely radial, as naively expected. A stretching and compression along the diagonals is seen. That is caused by

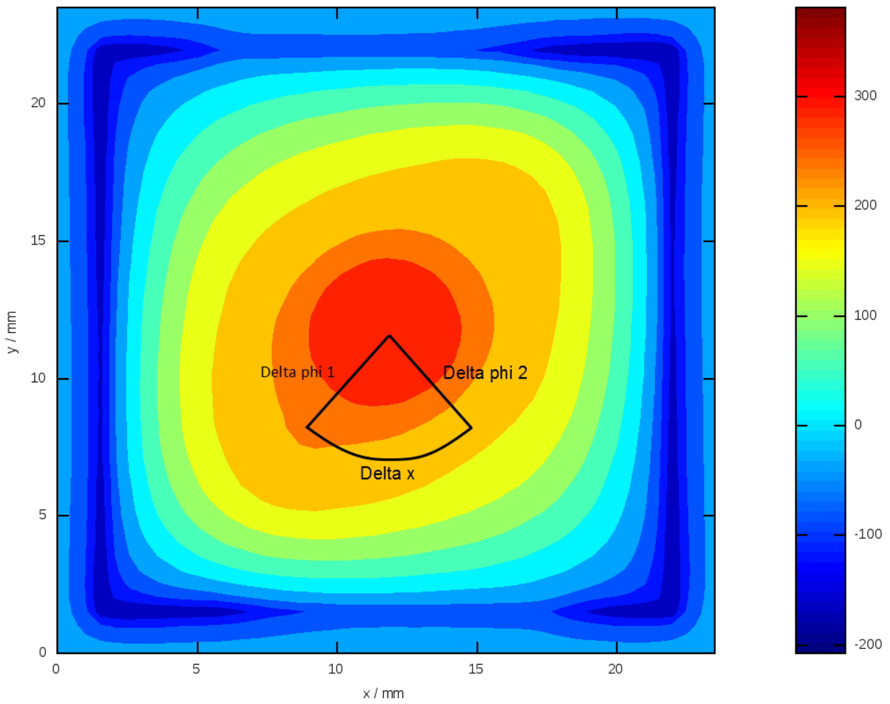

Figure 4.7.: Plasma potential(in V) of a HEMP thruster model in the $x-y-$plane at the cusp region $z = 20.5mm$.

azimuthal field fluctuations. One can identify a $n = 1$ mode oscillation at about $\phi = 250V$ and a $n = 2$ mode at about $\phi = 200V$. While no SEE is implemented in this model, only slight distortions of the system cause these fluctuations. One possible electromagnetic fluctuation is the so called flute instability. Here small waves become larger with time. It is also known as the RayleighTaylor instability in plasmas [18].

The electron density is shown in figure 4.8 and 4.9. The density profile for $y = L_y/2$, figure 4.8, shows a large electron density at the anode ($z = 0$) and at the anode cusp ($z = 20.5$). The density drop between the two regions is due to the electron transport along magnetic field lines. At the exit cusp, practically no electrons can be found, because it is not yet filled with charged plasma particles. Due to that, no negative wall potential for the exit cusp can be seen in figure 4.6.

In figure 4.9, the electron density in the x-y-plane at the anode cusp $z = 20.5mm$ is shown. A high electron density in the center of the model can be seen. Similar to the potential a slight stretching and compression along the diagonals is visi-

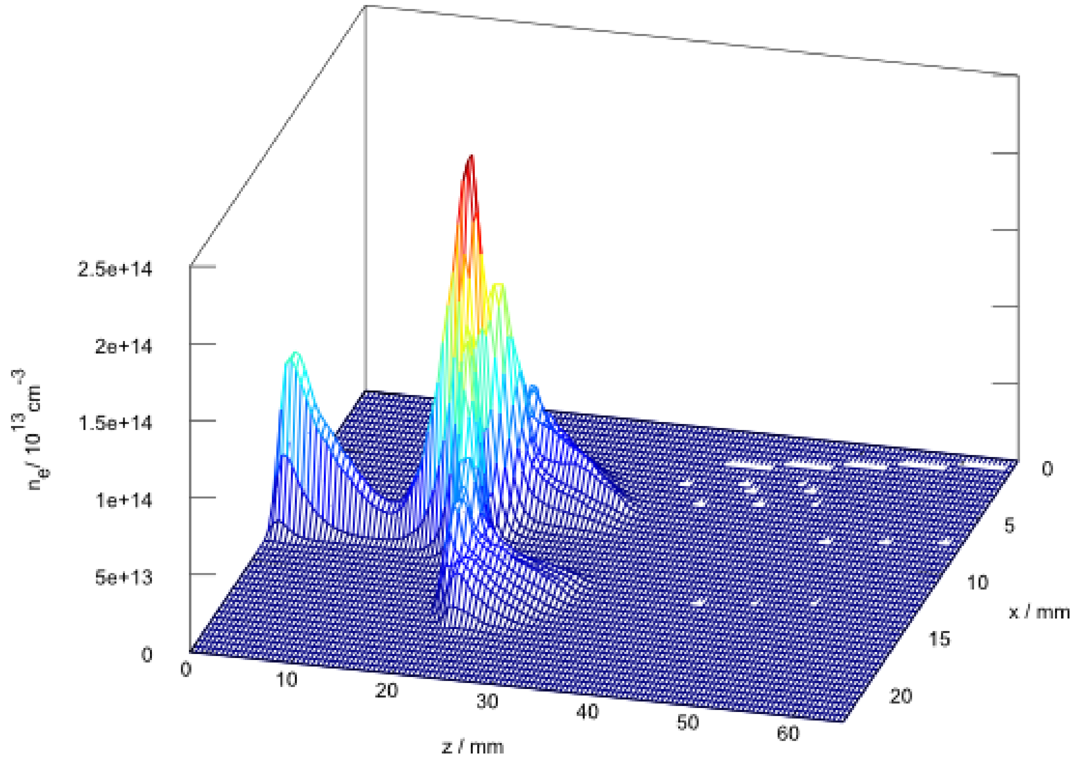

Figure 4.8.: Electron density along the y-axis of a HEMP thruster model at $y = 15.5mm$.

ble. While effects of the distorted plasma potential exists in the whole plasma volume, differences in one density slide (x-y-plane) are not very high. Rather small differences over the whole volume appear.

The asymmetric potential gives an anomalous transport perpendicular to the magnetic field line. To estimate the anomalous diffusion coefficient, the ratio of the potential distortion and spatial distance has to be measured. In [20] L. Spitzer gave the anomalous diffusion coefficient as

$$D = \frac{2\left\langle E^2\right\rangle}{B}\tau = 2(K_1K_2)^2K_3\frac{k_BT}{eB} \quad .$$

The constant $K_3 = \tau/\omega_c$ were given as equal to one for magnetized systems, while K_1 is determined by

$$\sqrt{\langle E^2\rangle} = K_1\frac{\Delta\phi}{r_L} \tag{4.4.2}$$

In figure 4.7, one can approximate the potential distortion due to the anomalous

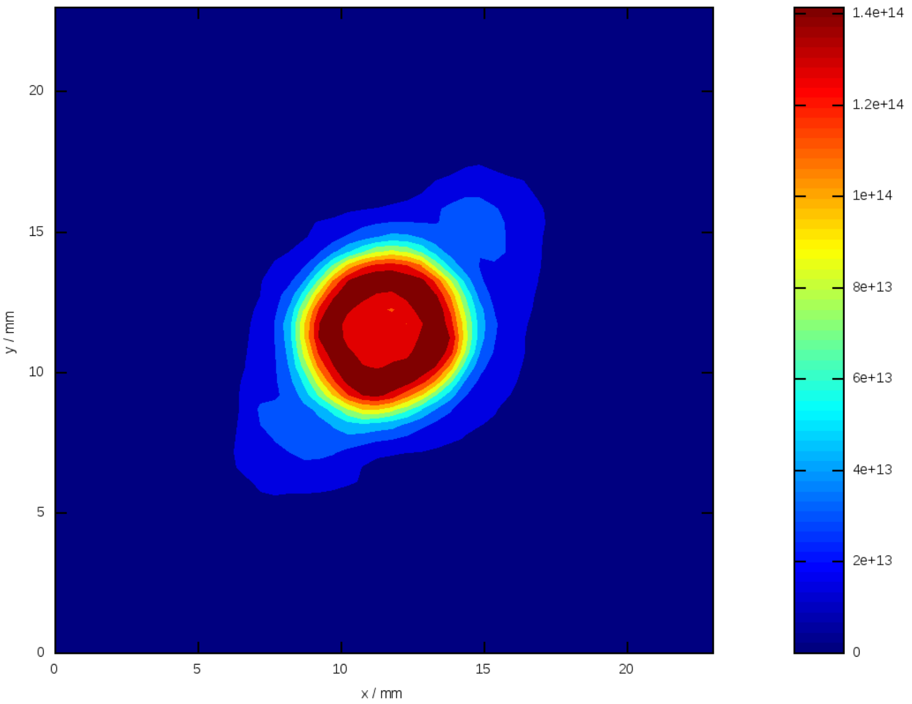

Figure 4.9.: Electron density (in cm^{-3}) of a HEMP thruster model in the $x-y-$plane at the cusp region $z = 20.5mm$.

diffusion as

$$\sqrt{\langle E^2 \rangle} \quad = \quad \frac{\Delta\phi}{\Delta x} = \frac{50eV}{20\lambda_D} \tag{4.4.3}$$

The third constant were defined by the equation

$$e\Delta\phi \quad = \quad K_2 k_B T \quad . \tag{4.4.4}$$

Combining equation 4.4.2 and 4.4.2 one gets the expression

$$\left(\frac{\Delta\phi}{\Delta x}\right)^2 \quad = \quad (K_1 K_2)^2 \left(\frac{k_B T}{r_L}\right)^2 \quad , \tag{4.4.5}$$

which gives the constant for the anomalous diffusion coefficient as

$$2 \cdot (K_1 K_2)^2 K_3 \quad = \quad \left(\frac{\frac{\Delta\phi}{k_B T}}{\frac{\Delta x}{r_L}}\right)^2 K_3 \quad . \tag{4.4.6}$$

For the present simulation, the domain were scaled [17], therefore a scaling factor of 50 has to be added. For the parameters $k_B T = k_B T_e = 10eV$, $\lambda_D = 4r_L$ and $K_3 = 1$, one gets for the factor of the anomalous diffusion

$$2 \cdot (K_1 K_2)^2 K_3 \cdot 50 = 2 \cdot \left(\frac{5}{80}\right)^2 \cdot 50 \approx \frac{2}{5} \quad ,$$

which is in the order of magnitude of the diffusion coefficient Bohm found. One has to mention, that the presented calculation is only a rough estimate, because the linear scaling of the potential of gradients with the domain size is not fully clear. Also the estimate $K_3 = \tau/\omega_c = 1$ is not provable, while the collision frequency is unknown.

5. Conclusions

This thesis used numerical simulations to study the physics of ion thrusters, namely for two specific types, the so-called Hall thruster SPT and the HEMP. Two major topics were covered, the problem of plasma-wall interaction and the problem of turbulence and its effect on transport fluxes. The major characteristics of plasmas and their interaction with walls is the dominance of non-linear physics driving waves and instabilities. After introducing the basic physics and the methods used to describe them numerically, the main operational differences between SPT and HEMP were shown, namely their difference in the potential distribution in the acceleration channel. The SPT is characterized by a nearly linear potential drop, whereas HEMP has a nearly constant plasma potential with a steep drop at the exit zone. These differences result in very different erosion characteristics due to energetic ions hitting the walls: the SPT shows rather strong erosion, whereas HEMP has nearly negligible one. For the qualification of ion thrusters for space missions the interaction of the produced ions in the plume region with test vessel walls has to be minimized, because back-flow of impurities generated by this process can produce artifacts in thrust measurements and angular distributions of the thruster. Simulations for the calculations of back-flows of impurities back to the thruster from the vessel walls are presented using both Monte-Carlo and analytical approaches. Both agree very well and support the results. Based on these models implementation of tilted baffles in testing devices are proposed, which will be realized soon in industry. Plasma-wall instabilities created from the non-linear response of the plasma sheath and its modification from SEE are discussed. A specific example, how wall instabilities can affect the whole plasma and determine its turbulence and subsequent so-called anomalous transport is presented for SPT. Strong SEE can lead here to an unstable plasma sheath creating strong fluctuations in the electric field and emission of beam-like secondary electrons transferring between the two cylinders of the SPT. This creates elongated filamentary structures in the potential producing anomalous transport in analogy of a kicked rotor. For HEMP, a fully 3D kinetic simulation using the Particle-in-Cell method allows the self-consistent analysis of electrostatic turbulence even without SEE only due to the non-linear response of the plasma sheath. An estimate of the anomalous diffusion flux resulting from this turbulence was done and the same order of magnitude was found as the well-known Bohm diffusion. For the numerical optimization of such calculations the performance of a parallel solver based on the matrix solver package SuperLU_Dist was evaluated. Unfortunately, it is impossible to reduce the calculation time for the back-solve below 5 seconds, which is still too costly for 3D calculations.

The physics and simulations of ion thrusters is a fascinating topic with plenty of interesting questions to be addressed. This thesis can only be an appetizer for this, but it tries to contribute to an improved understanding of the basic effects needed for a real optimization of such systems. A lot of work remains to be done, but also progress is made towards the ultimate goal of a predictive model.

A. Appendix

A.1. The Bohm criteria

The Bohm criteria, which gives an estimate of the flow velocity of the in streaming ions on the sheath, is a one-dimensional effect and therefore we will look just at the x coordinate which is perpendicular to the wall.

In the sheath area with $x_s > x > \lambda_D$ the potentialdrop can be seen as small $\Delta\phi = \Phi_{pl} - \Phi_W \ll k_B T_e$ for cold ions and hot electrons. Due to the reflected electrons from the wall, the electron density in this region is given as a Maxwell-Boltzmann-distribution

$$n_e(x) = n_{e,pl} \cdot exp\{-\frac{e\Delta\phi}{k_B T_e}\} \;\approx\; n_{e,pl}(1 - \frac{e\Delta\phi}{k_B T_e}) \tag{A.1.1}$$

From the energy conservation of the ions: $\frac{1}{2}m_i\vec{v}_{i,Pl}^2 = \frac{1}{2}m_i\vec{v}_i^2 - e\Delta\phi$ one gets

$$\vec{v}_i^2 = \vec{v}_{i,pl}^2 + 2\frac{e}{m_i}\Delta\Phi \tag{A.1.2}$$

Combining these equation with conservation of the current density of the ions: $n_{i,pl}v_{i,pl} = n_i v_i$ one gets for the ion density

$$n_i(x) = n_{i,pl}\sqrt{\frac{v_{i,pl}^2}{v_{i,pl} + 2e\Delta\phi/m_i}} \;\approx\; n_{i,pl}(1 - \frac{e\Delta\phi}{m_i v_{i,pl}^2}) \tag{A.1.3}$$

Since we are looking at the sheath region of the plasma, we can expect a small nettocharge $0 \leq n_i(x) - n_e(x)$ so that we can get the Bohm criteria by entering the densities

$$v_{i,pl} \geq \sqrt{\frac{k_B T_e}{m_i}} \tag{A.1.4}$$

A.2. Monte Carlo Sampling

The Monte Carlo sampling is a simple method to sample a given distribution function with uniformly distributed random numbers.
Suppose the random variable Y should be sampled in N random samples $\{y_i\}_{i=1}^N$, distributed with the given probability distribution function $f_Y(y)$. For any other distribution function of a random variable X the following equality is valid:

$$f_X(x)dx \quad = \quad f_Y(y)dy \ . \tag{A.2.1}$$

If X is uniformly distributed in the range $[0;1]$

$$f_X(x) = \begin{cases} 1, & 0 \leq x \leq 1 \\ 0, & else \end{cases}$$

the integration of equation A.2.1 gives

$$x = \int_{-\inf}^{y} f_Y(\tilde{y})d\tilde{y} = F_Y(y)$$

with the cumulative distribution function $F_Y(y)$. The application of the inverse cumulative distribution function $F_Y^{-1}(y)$ then gives the Monte Carlo sampling of the variable Y with a given distribution $F_Y(y)$, by the uniformly distributed numbers x

$$y \quad = \quad F_Y^{-1}(x) \ . \tag{A.2.2}$$

Bibliography

[1] E. Messerschmid and S. Fasoulas. Raumfahrtsysteme, Eine Einführung mit Übungen und Lösungen, vol. third. Springer Verlag **2009**

[2] J. Bittencourt. Fundamentals of Plasma Physics. Springer Verlag, 3rd edn. **2004**

[3] R. Schneider. Plasma edge physics for tokamaks

[4] G. D. Hobbs and J. A. Wesson. Heat flow through a langmuir sheath in the presence of electron emission. Plasma Physics, 9(1) 85 **1967**

[5] M. A. Lieberman and A. J. Lichtenberg. Principles of Plasma Discharges and Materials Processing. Wiley-Interscience, 2nd edn. **2005**

[6] F. Taccogna, S. Longo, M. Capitelli *et al.* Particle-in-cell simulation of stationary plasma thruster. Contributions to Plasma Physics, 47(8-9) 635–656 **2007**. doi:10.1002/ctpp.200710074

[7] D. Tskhakaya, K. Matyash, R. Schneider *et al.* The particle in cell method. Contrib Plasma Phys, 47(8-9) 563–594 **2007**

[8] J. P. Boris and R. A. Shanny, eds. Proceedings of the Fourth Conference on Numerical Simulation of Plasmas. Naval Research Laboratory **1971**

[9] J. W. Demmel, S. C. Eisenstat, J. R. Gilbert *et al.* A supernodal approach to sparse partial pivoting. SIAM J Matrix Analysis and Applications, 20(3) 720–755 **1999**

[10] K. Matyash. Kinetic Modeling of Multi-Component Edge Plasmas. Ph.D. thesis, Ernst-Moritz-Arndt-Universität Greifswald **2003**

[11] T. Takizuka and H. Abe. A binary collision model for plasma simulation with a particle code. J Comp Phys, 25 205–219 **1977**

[12] M. Furman and M. Pivi. Probabilistic model for the simulation of secondary electron emission. Physical Review Special Topisca-Accelerators and Beams, 5(12) **2002**. doi:10.1103/PhysRevSTAB.5.124404

[13] R. M. A. S. R. Eckstein, W.; Dohmen. Sdtrimsp: A monte-carlo code for calculating collision phenomena in randomized targets. IPP Report, 12/3 40 **2007**

[14] W. Eckstein. Computer Simulation of Ion-Solid Interaction, vol. 10 of *Springer Series in Material Science*. Springer **1991**

[15] N. Koch, H.-P. Harmann and G. Kornfeld, eds. Status of the THALES High Efficiency Multi Stage Plasma Thruster Development for HEMP-T 3050 and HEMP-T 30250, IEPC-2007-110. Florence, Italy **2007**

[16] G. Kornfeld, H. Seidel and J. Wegener. Plasma accelerator arrangement **1999**. Priority: Germany No. 198 28 704.6, filed 26 June 1998

[17] K. Matyash, R. Schneider, A. Mutzke *et al.* Kinetic simulations of spt and hemp thrusters including the near-field plume region. IEEE Transactions on Plasma Since, 38(9, Part 1) 2274–2280 **2010**. doi:10.1109/TPS.2010.2056936

[18] F. F. Chen. Introduction to Plasma Physics and Controlled Fusion, Volume 1: Plasma Physics, vol. 1. Springer Verlag **1984**

[19] R. Hockney and J. Eastwood. Computer simulation using particles. Adam Hilger **1981**

[20] L. Spitzer. Particle diffusion across a magnetic field. Physics of fluids, 3(4) 659–661 **1960**. doi:10.1063/1.1706104

[21] F. Taccogna, S. Longo, M. Capitelli *et al.* Anomalous transport induced by sheath instability in hall effect thrusters. Applied Physics Letters, 94(25) **2009**. doi:10.1063/1.3152270

[22] C. K. Birdsall and A. B. Langdon. Plasma physics via computer simulation **1985**

[23] J. Argyris, G. Faust, M. Haase *et al.* Die Erforschung des Chaos. Springer Verlag **1995**

[24] Private communication with K. Matyasch

Danksagung

Hiermit möchte ich mich bei Professor R. Schneider bedanken, für seine Unterstützsung uns Hilfe bei der Erstellung dieser Diplomarbeit. Auch möchte ich K. Matyash, L. Lewerenz, sowie der gesamten Arbeitsgruppe "Computaional Physics" der Ernst Moritz Arnd Universität Greifswald für die vielen interessanten Diskussionen und die angenehme Arbeitsatmosphäre danken.
Des weiteren bedanke ich mich bei Professor M. Bestehorn, für seine Unterstützung bei der Realisierung meines Aufenthalts als Gaststudentin an der Ernst Moritz Arnd Universität Greifswald. Mein Dank geht nicht zuletzt auch an T. Latzel und meine Familie, deren geistige und finanzielle Unterstützung mein Studium erleichterte und beeinflusste.